Check for updates

JGR Space Physics

RESEARCH ARTICLE
10.1029/2022JA030602

Key Points:

- Two moderate geomagnetic storms with similar solar wind conditions produced MeV electron dropouts of different flux levels in the outer belt
- Radial diffusion simulations performed for the case studies using event-specific D_{LL} capture the main phase dropouts above $L^* = 4.5$
- Stronger outward radial diffusion loss or additional mechanism is needed to explain losses down to $L^* < 4.5$ in the strong dropout case

Supporting Information:

Supporting Information may be found in the online version of this article.

Correspondence to:

G. B. D. Silva,
graziela.silva@inpe.br

Citation:

Silva, G. B. D., Alves, L. R., Tu, W., Padilha, A. L., Souza, V. M., Li, L.-F., et al. (2022). Modeling radiation belt electron dropouts during moderate geomagnetic storms using radial diffusion coefficients estimated with global MHD simulations. *Journal of Geophysical Research: Space Physics*, *127*, e2022JA030602. https://doi.org/10.1029/2022JA030602

Received 30 APR 2022
Accepted 22 JUL 2022

Author Contributions:

Conceptualization: G. B. D. Silva, L. R. Alves, A. L. Padilha
Data curation: G. B. D. Silva, V. M. Souza
Formal analysis: G. B. D. Silva, L. R. Alves, W. Tu, A. L. Padilha, V. M. Souza, L.-F. Li, X. Lyu
Funding acquisition: L. R. Alves
Investigation: G. B. D. Silva, L. R. Alves, W. Tu, A. L. Padilha
Methodology: G. B. D. Silva, L. R. Alves, W. Tu, A. L. Padilha, V. M. Souza
Project Administration: L. R. Alves, A. L. Padilha
Resources: L. R. Alves, W. Tu, A. L. Padilha

© 2022. American Geophysical Union. All Rights Reserved.

Modeling Radiation Belt Electron Dropouts During Moderate Geomagnetic Storms Using Radial Diffusion Coefficients Estimated With Global MHD Simulations

G. B. D. Silva[1], L. R. Alves[1], W. Tu[2], A. L. Padilha[1], V. M. Souza[1], L.-F. Li[3], X. Lyu[2], and M. B. Pádua[1]

[1]National Institute for Space Research (INPE), Sao Jose dos Campos, Brazil, [2]Department of Physics and Astronomy, West Virginia University, Morgantown, WV, USA, [3]Institute of Mechanics, Chinese Academy of Science, Beijing, China

Abstract Main phase flux dropouts often promote depletion of the outer electron radiation belt. The quantification of the contributions of various loss mechanisms to MeV electron dropouts has not yet been elucidated in detailed case studies for moderate geomagnetic storms. This work focuses on quantifying radial diffusion to study relativistic electron flux losses observed by Van Allen Probes during two moderate storms in 2017. The events are identified as Case 1 (27 March), with losses deep in L, and Case 2 (21 November), with less deep losses. Event-specific radial diffusion coefficients (D_{LL}) were calculated from global magnetohydrodynamic (MHD) fields simulated by the SWMF/BATS-R-US. The MHD-D_{LL} was used as an input to radial diffusion simulations of both events for relativistic electrons. For the outer boundary conditions defined at $L^* = 6$, electron fluxes measured by GOES-15 at geosynchronous orbit were converted to phase space densities (PSDs) and then calibrated against the Van Allen Probe A measurements. Using these calibrated PSD of GOES-15 at the outer boundary and event-specific MHD-D_{LL}, the main phase dropout is well captured with radial diffusion simulation for Case 2, but not for the deep dropout in Case 1 down to $L^* < 4.5$. Scaling MHD-D_{LL} based on validations of the MHD waves against in situ wave observations improves the simulation results of Case 1, but still does not fully resolve its deep dropout. However, analyzing the uncertainty of simulated PSD imposed by the uncertainty in the scaled MHD-D_{LL}, it was found that outward radial diffusion could still account for the losses at $L^* < 4.5$.

1. Introduction

The Earth's outer radiation belt hosts geomagnetically trapped relativistic and ultra-relativistic electrons of highly dynamic fluxes located mainly at $L = 3$–7. These populations of penetrating particles are hazardous to spacecraft electronic systems in space (e.g., Baker et al., 2018). It is well established that flux variability in the outer belt arises from the significant loss and acceleration of these electrons usually associated with active geomagnetic conditions. These dynamic mechanisms may lead to the occurrence of a flux dropout or flux enhancement, or even no flux changes in case of a balance between loss and acceleration processes (Reeves et al., 2003).

The sudden depletion or even extinction of radiation belts affecting several energy levels and L shells defines a flux dropout (Olifer et al., 2018; Ozeke et al., 2017; Turner, Morley, et al., 2012; Xiang et al., 2017, 2018). They often occur during the main phase of storms (e.g., Turner et al., 2019) and, if related to actual ongoing electron losses rather than just adiabatic effects, can mainly result from sudden losses to magnetopause. This happens through an enhanced compression of this boundary in conjunction with outward radial diffusion and deceleration of electrons (e.g., Alves et al., 2016; Hudson et al., 2014; Loto'Aniu et al., 2010; Turner, Shprits, et al., 2012; Tu et al., 2019). Flux dropouts can also result from electron precipitation into the atmosphere induced by wave-particle resonant interactions with several high-frequency plasma waves (Pham et al., 2017; Schulz & Lanzerotti, 1974; Thorne, 2010; Tu et al., 2010). The main phase dropout may be followed by a flux recovery of MeV electrons as a result of inward radial diffusion or local acceleration acting on seed populations due to whistler-mode chorus wave interactions during substorms (Green & Kivelson, 2004; Jaynes et al., 2015; Summers et al., 1998; Tu et al., 2014).

Radial diffusion is thus a key mechanism for driving flux dropouts and recovery of radiation belt electrons. It is mediated mainly by ultra-low frequency (ULF) waves in the Pc5 range (~2–7 mHz; Jacobs et al. [1964]) propagating eastward as the drift motion of electrons around an L shell (Elkington, 2006). Once the electrons' third

Software: G. B. D. Silva, W. Tu, M. B. Pádua
Supervision: L. R. Alves, W. Tu, A. L. Padilha
Validation: G. B. D. Silva, W. Tu, V. M. Souza, L.-F. Li, X. Lyu
Visualization: G. B. D. Silva
Writing – original draft: G. B. D. Silva
Writing – review & editing: G. B. D. Silva, L. R. Alves, W. Tu, A. L. Padilha

adiabatic invariant is violated through this resonant and stochastic interaction, they become free to move inward (outward) across L shells, which increases (decreases) the electron energy due to the conservation of the first invariant. Outward radial diffusion in conjunction with magnetopause shadowing has been invoked to explain electron dropouts near the magnetopause down to the Global Positioning System (GPS) orbit at $L^* \geq 4$ (Olifer et al., 2018), where L^* is the Roederer's L (quantity inversely proportional to the third invariant; Roederer [1970]). But $L^* \sim 4$ is also the altitude that wave-induced precipitation of MeV and multi-MeV electrons are likely to be enhanced during magnetic storms and result in rapid localized electron dropouts, especially for the multi-MeV regime, due to interactions with electromagnetic ion cyclotron (EMIC) waves (e.g., Shprits et al., 2017; Summers et al., 1998). Previous numerical simulations based on 1D (Ozeke, Mann, Turner, et al., 2014) and 3D (Drozdov et al., 2015) radiation belt diffusion codes were generally able to capture dropouts of ∼MeV electrons over storm time and across L shells. These works simulated mainly the major loss effects from magnetopause shadowing and outward radial diffusion, together with gradual loss effects such as driven by whistler-mode chorus and hiss waves (e.g., Orlova et al., 2014; Shprits et al., 2007). For instance, Ozeke, Mann, Turner, et al. (2014) simulated a long-term interval of the quiet year of 2008, while Drozdov et al. (2015) simulated a one-year period over 2012–2013 related to a solar maximum. However, the relative contribution of magnetopause shadowing and EMIC wave scattering during individual dropout events has not yet been resolved.

The interval of high solar activity marks a period of intensified occurrence of interplanetary coronal mass ejections (ICMEs) in the solar wind, whereas in the interval of low solar activity there is a rise in the formation of corotating interaction regions (CIRs) throughout the heliosphere (for an overview, refer to Richardson [2018]). ICMEs and CIRs are known to be the main drivers of geomagnetic storms (e.g., Tsurutani et al. (2006)). The effectiveness of each of these solar wind structures for generating flux variations in the outer radiation belt has been studied widely (e.g., McPherron et al., 2009; Morley et al., 2010; C. Yuan & Zong, 2013); C.-J. Yuan et al., 2015; Turner et al., 2019). It is still challenging to simulate the responses of the outer radiation belt to the geomagnetic conditions imposed by ICMEs and CIRs in case studies. In this context, case studies simulating electron dropouts under moderate geomagnetic storms are still scarce in the literature, with some attempts using magnetohydrodynamic (MHD)-test particle runs (Hudson et al., 2012, 2021). Also, Yu et al. (2013) inserted superposed epoch conditions from 67 high-speed stream minor storms into a radial diffusion code to model relativistic electron flux dropouts, which were compared with GPS observations spanning $4 \leq L^* \leq 7$. The simulations reproduced well magnetopause shadowing and outward diffusive loss at high L shells but were limited in reproducing dropouts at inner L regions. This limited result for low L was mainly attributed to the lack of atmospheric loss in the simulations.

Conversely, the general role of fast outward radial diffusion in relativistic electron dropouts has been well characterized numerically in more intense storm-time periods related to ICMEs (Alves et al., 2016; Hudson et al., 2014; Z. Li et al., 2014; Ozeke et al., 2017; Shprits et al., 2006). A fundamental difference between stronger storms, when compared to weaker events, is that the magnetopause shadowing can dominate the sudden deep losses into the outer belt if the last closed drift shell (LCDS) reaches values as low as $L^* = 4$. Subsequently, the greater effect of this mechanism induces very rapid outward diffusion of electrons, which can completely deplete the belt. This was the case for the June 2015 superstorm simulated by Tu et al. (2019). Using a radial diffusion code, these authors were able to capture well the dominant magnetopause shadowing responses observed by Van Allen Probes on MeV and multi-MeV electron fluxes during that storm. Another example is the dropout event following the March 2013 intense storm with minimum LCDS ∼5 (see Olifer et al. [2018]), also resolved with radial diffusion simulation for several MeV energies without considering EMIC waves (Ozeke et al., 2020). However, the role of outward radial diffusion in radiation belt dropout during less intense CIR storms has not yet been well quantified in event studies.

On the other hand, the radial diffusion coefficient (D_{LL}) of an electron with a certain drift frequency depends mainly on the power spectrum and azimuthal mode structure of the ULF waves (Falthammar, 1965; Tu et al., 2012). In order to quantify electron radial diffusion rates over storm time, several methods have been established. They include the statistical representations for D_{LL} based on the Kp index and long-term satellite, and ground-based ULF wave measurements (Ali et al., 2016; Brautigam & Albert, 2000; Liu et al., 2016; Ozeke, Mann, Murphy, et al., 2014). More recently, event-specific estimates of D_{LL} coefficients were derived using similar databases and making assumptions for the azimuthal mode numbers (Mann et al., 2016; Olifer et al., 2019; Ozeke et al., 2020; Sandhu et al., 2021), or physically resolving them (Barani et al., 2019). Additionally, more robust

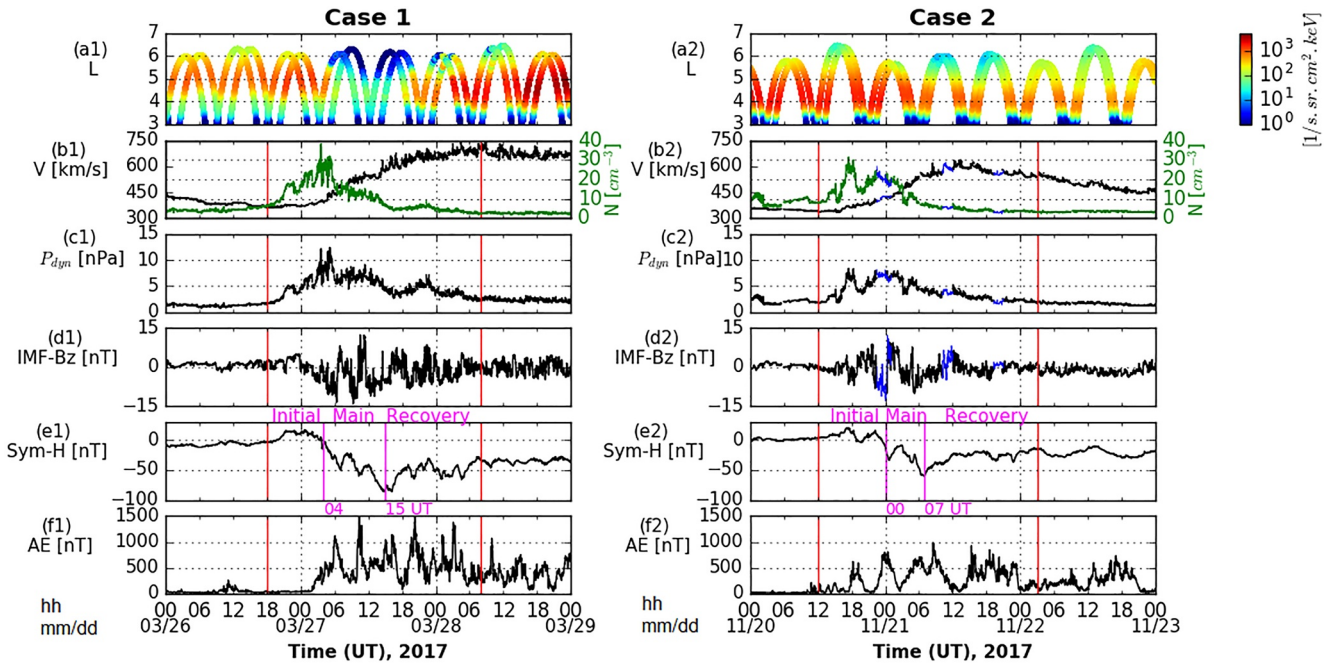

Figure 1. Overview of radiation belt electron fluxes observed by Van Allen Probes and upstream solar wind conditions and geomagnetic activity from OMNIWeb, during 26–28 March 2017 (case study 1) and 20–22 November 2017 (case study 2). (From top to bottom) Temporal and radial distribution of electron fluxes at 1.8 MeV and 90° local pitch angle; solar wind flow velocity overplotted with density (black and green curves, respectively); dynamic pressure; B_z component of the interplanetary magnetic field (IMF); geomagnetic index SYM-H with indication and timing of the storm phases, and the AE index. In panels b2–d2, gaps in the OMNI data have been filled in with cleaned DSCOVR observations shown in blue. Red vertical lines delimit the interval of magnetohydrodynamic simulations.

ways of quantifying D_{LL} can be achieved using global MHD simulations (Fei et al., 2006; Huang et al., 2010; Tu et al., 2012; Z. Li et al., 2017; L.-F. Li et al., 2020). Many previous studies of storm-time D_{LL} based on MHD simulations have focused on describing the mode structure associated with the derived radial diffusion coefficients (Fei et al., 2006; Z. Li et al., 2016; L.-F. Li et al., 2020; Tu et al., 2012). These studies indicated an advantage of the MHD approach over the others previously mentioned since D_{LL} rates are consistently obtained from global electric and magnetic fields in a large spectrum of mode numbers, m. Large-scale waves have $m \to 0$, and small-scale waves conversely have $m \to \infty$. In this way, simulated ULF waves at different azimuthal scales, while satisfying the drift resonance condition, can be taken into account in the D_{LL} estimation from MHD.

Furthermore, previous works such as Tu et al. (2019) have also shown that the simulated magnetopause shadowing loss is very sensitive to the radial diffusion rate used so physically quantified D_{LL} is critical to simulate radiation belt electron dropouts. Thus, we are motivated in this work to develop event-specific D_{LL} to model radiation belt electron dropouts in case studies of CIR storms, and quantify mainly the contribution of magnetopause shadowing and outward radial diffusion mechanisms to these losses. We use a global MHD model to compute the event-specific D_{LL} and evaluate the impact of two moderate storms (-100 nT $\leq Dst \leq -50$ nT) driven by CIRs in 2017 on a relativistic electron population. The main goal is to elucidate, from the perspective of the storm-time behavior of the event-specific diffusion rates, why similar CIR events generated a stronger and deeper flux dropout during the 27 March 2017 event in comparison to the 21 November 2017 event. Radial diffusion simulations employing diffusion coefficients from MHD are carried out for the two case studies, with detailed information about the events and the radial diffusion analysis and simulation methods used given next.

2. Events Overview

The main objective of this study is to analyze two CIR-driven storms in 2017 that promoted different dropout dynamics in the outer radiation belt. The proposed approach for investigating both dropout events is based on global MHD simulations of the magnetosphere in conjunction with radial diffusion modeling of the trapped relativistic electron populations. Figure 1 shows an overview of the solar wind conditions and geomagnetic activity during a 3-day interval of observations of radiation belt electron fluxes by NASA Van Allen Probes (formerly

Radiation Belt Storm Probes (RBSP)) on March 26–28, 2017 (left panels) and on November 20–22, 2017 (right panels). Following in this text, each interval will be identified as case study 1 and case study 2, respectively. In panels a1 and a2, the 1.8 MeV electron fluxes at 90° local pitch angle were measured by the Relativistic Electron-Proton Telescope (REPT) detectors (Baker et al., 2013), onboard the Van Allen Probes (RBSP-A and RBSP-B), are given as a function of time and the McIlwain L (McIlwain, 1961). Panels b1–f1 and b2–f2 sequentially display the solar wind parameters and geomagnetic indices obtained from OMNIWeb as follows: the solar wind speed in black overplotted with the proton bulk density in green, dynamic pressure, interplanetary magnetic field (IMF) B_z component and geomagnetic indices SYM-H and AE. Specifically, panels b2–d2 have the OMNI data for Case 2 filled in with cleaned L1-point observations by DSCOVR, which are shown in blue in the OMNI data gaps. DSCOVR data were also taken from OMNIWeb (https://omniweb.gsfc.nasa.gov/ftpbrowser/dscovr_merged.html). The vertical red lines on all panels depict the period chosen for the MHD simulations.

It can be seen in Figure 1 (panels a1–f1) that the flux dropout of Case 1, starting at ∼4 UT on 27 March, was concurrent with the passing of a compression region in the solar wind, associated with intense dynamic pressure of >10 nPa (see panel c1). Meanwhile, a moderate storm took place along with the enhanced substorm activity, as shown in panels e1–f1. It is noted that this fast-flux dropout reached the entire outer belt, as deep as $L \sim 4$, and recovered around 18 UT on 27 March. In Case 2 (panels a2–f2), the flux dropout observations start at ∼6 UT on 21 November. It occurred following a compression region with slightly less enhanced values in the solar wind parameters (e.g., the dynamic pressure peak was <10 nPa as seen in panel c2). It can be noted that the flux dropout of Case 2 is very mild (i.e., representing a flux decay ≤ one order of magnitude around $L = 6$ against the 1–2 orders of flux decay for Case 1), and hence ∼1 R_E less deep compared to that of Case 1. In addition, the electron fluxes do not recover to values higher than those of prestorm, as observed in Case 1. Furthermore, lower levels of geomagnetic activity are identified in panels e2–f2 for this case (e.g., SYM-H minimum of −60 nT for Case 2 vs. −86 nT for Case 1), although the magnetic storm developed is also moderate.

The time intervals selected for the MHD simulations of the case studies, marked by the red vertical lines in Figure 1, cover the complete passage of the CIRs through the magnetosphere, which is when a significant compression of the dayside magnetopause is expected (e.g., Morley et al. (2010)). In addition, the period following the passage of the CIRs, which concerns the high-speed streams' driving in the magnetosphere, was also taken into account in the MHD simulations. In terms of storm phases, these intervals have been entirely defined from the initial storm phase to the early recovery phase. Such phases identified in panels e1 and e2 were defined following the instructions in Tsurutani et al. (2006), which are appropriate for the case of CIR storms (see Figure 10 of this former paper). Most importantly, these definitions for the initial and main phases facilitate the analysis of the SYM-H in Case 2, which peaks twice for positive disturbed values before entering the main phase of the storm. The magnetic storms ended on 3 April for Case 1 and on 24 November for Case 2.

2.1. MHD Simulations

The Space Weather Modeling Framework/Block-Adaptive Tree Solar-Wind Roe-Type Upwind Scheme (SWMF/BATS-R-US) global MHD model (Tóth et al., 2005, 2011), coupled with the Comprehensive Inner-Magnetosphere Ionosphere (CIMI) model (Fok et al., 2014), constitutes the numerical approach used here to study the global interaction of the two CIRs with the Earth's magnetosphere. Runs based on these coupled models of version v20180525 were carried out upon request at the Community Coordinated Modeling Center (CCMC; https://ccmc.gsfc.nasa.gov/). In a similar approach, Alves et al. (2017) used SWMF/BATS-R-US to investigate the activity of ULF wave propagation modes in the magnetosphere under two different solar wind transients, also focusing on the description of the outer belt electron dynamics. The reader is referred to this previous article and Tóth et al. (2011) for a complete overview of the global magnetosphere (GM), inner magnetosphere (IM), and ionospheric electrodynamics (IE) modules available in SWMF, as well as their coupling throughout the extension of the modeled magnetosphere from −250 R_E (Earth radii) to 33 R_E along the Sun-Earth line.

Solar wind data provided by the ACE and DSCOVR satellites were used to derive the outer boundary conditions of the simulation domain in cases 1 (the 27 March 2017 dropout) and 2 (the 21 November 2017 dropout). The inner boundary was set at 2.5 R_E, and a fine grid resolution of 0.25 R_E was set to fill a domain closest to Earth, defined as $-32 \leq x \leq 24$, $-24 \leq y \leq 24$, and $-20 \leq z \leq 20$ R_E in both runs. Coordinates and output fields are given in the geocentric solar magnetospheric (GSM) system. In an attempt to acquire more realistic MHD fields for the D_{LL} calculations, the simulated global magnetic fields were configured to present a dipole tilt in the X–Z

plane of 12.96° for Case 1 and −29.66° for Case 2, which have been updated over time. The output data obtained in the runs have a 1-min cadence so that the output frequencies range up to 8.33 mHz, which allows analyzing the global activity of ULF waves in the Pc5 band. This class of ULF waves is well known to be responsible for the radially diffusive loss and acceleration of electrons in the outer belt (e.g., Elkington [2006]; Shprits et al. [2008]). The total duration of the MHD simulations was 38 hr for Case 1 and 39 hr for Case 2.

3. ULF Wave Radial Diffusion Analysis

Gradual changes in phase space density (PSD) of radiation belt electrons driven by radial diffusion are related to the magnitude of their radial diffusion rates (D_{LL}), which can be represented by:

$$D_{LL} = \frac{\left\langle (\Delta L)^2 \right\rangle}{2t}, \tag{1}$$

where D_{LL} represents the mean squared displacement of the radiation belt particles over a timescale t much greater than their drift period (e.g., Tu et al. (2012)), being commonly given in units of [day^{-1}]. Assuming equatorially-mirroring relativistic electrons, the contribution from ULF wave resonance modes to D_{LL} is quantified as (Fei et al., 2006):

$$D_{LL}^{E} = \frac{L^6}{8B_E^2 R_E^2} \sum_m P_m^E \left(m\omega_d\right), \tag{2}$$

$$D_{LL}^{B} = \frac{\mu^2 L^4}{8e^2\gamma^2 B_E^2 R_E^4} \sum_m m^2 P_m^B \left(m\omega_d\right), \tag{3}$$

$$D_{LL} = D_{LL}^{E} + D_{LL}^{B}, \tag{4}$$

where D_{LL}^{E} and D_{LL}^{B} are the resulting electric and magnetic radial diffusion coefficients, respectively, whose sum gives the total D_{LL} as shown in Equation 4. They are proportional to the sum of the power spectral densities ($P_m^E\left(m\omega_d\right)$ and $P_m^B\left(m\omega_d\right)$ terms) of the ULF waves in the azimuthal electric field and the compressional magnetic field components, taken at frequencies ω that satisfy the following drift-resonance condition:

$$\omega = m\omega_d, \tag{5}$$

where ω is the wave frequency, m is the associated azimuthal mode number, and ω_d is the bounce-averaged drift frequency of the electrons. In Equations 2 and 3, L represents the adopted model for drift shell (e.g., dipole L), B_E is the equatorial strength of the Earth's magnetic field at the surface, e is the electron charge, and γ is the Lorentz relativistic factor. A random correlation between electric and magnetic disturbances is assumed in this formalism (Lejosne & Kollmann, 2020).

For this calculation it is also essential to know the drift frequency at a given L on the equator, which for 90° pitch angle electrons and a given first invariant μ is expressed as:

$$\omega_d = \frac{-3\mu}{e\gamma\left(LR_E\right)^2} \tag{6}$$

in which a pure dipole magnetic field has been assumed (Ozeke, Mann, Murphy, et al., 2014).

3.1. D_{LL} Coefficients From Global MHD Fields

We followed the method discussed in detail by Tu et al. (2012) to obtain the D_{LL} coefficients using MHD-derived electric and magnetic fields. In this approach, the E_ϕ and B_z fields along circular orbits at the solar magnetic (SM) equator were initially derived. These circular orbits represent the electrons drift orbits in which D_{LL} rates were calculated, assuming the geomagnetic field as a dipole. Both field components are relevant to ULF wave fluctuations that account for the radial diffusion of radiation belt electrons, as defined in Equations 2–4.

Throughout the simulation process, the MHD fields were interpolated to a polar grid of 48 uniform azimuthal locations ϕ, along the circular drift orbits. These circular orbits were placed at radial distances r = 3–9 R_E, with

a 0.1 R_E grid separation. Along with the interpolation step, coordinate transformations from SM to GSM were performed since BATS-R-US inputs/outputs must be in GSM. Subsequently, the GSM fields were transformed back to SM, as follows. The input locations of the circular orbits, defined as ($x = r\cos\phi$, $y = r\sin\phi$, and $z = 0$) in the SM-equatorial plane, were changed to GSM coordinates (x', y', and z'), with the field components also interpolated in GSM. Subsequently, the GSM fields were transformed into SM fields corresponding to the previous coordinates ($x = r\cos\phi$, $y = r\sin\phi$ and $z = 0$) at the SM equator. To finalize the process, the SM (Cartesian) electromagnetic fields were transformed into cylindrical coordinates, so that the field components of interest, defined as E_ϕ (r, ϕ, t) and B_z (r, ϕ, t), could be derived. For these 2D interpolation steps and coordinate transformations, the *CCMC Kameleon* software with libraries written in Python was used (publicly available at https://ccmc.gsfc.nasa.gov/Kameleon/).

Then an FFT was computed along the azimuthal angle (ϕ - equal to zero at noon magnetic local time) to solve for the instant mode structure of ULF fluctuations at each r value, in the form:

$$E_\phi(r,\phi,t) = \sum_{m=1}^{\infty} E^a_{\phi,m}(r,t)\cos m\phi + \sum_{m=1}^{\infty} E^b_{\phi,m}(r,t)\sin m\phi, \tag{7}$$

$$B_z(r,\phi,t) = \sum_{m=1}^{\infty} B^a_{z,m}(r,t)\cos m\phi + \sum_{m=1}^{\infty} B^b_{z,m}(r,t)\sin m\phi. \tag{8}$$

where indices a and b indicate the real and imaginary counterparts of the FFT signals, respectively.

Over the m-resolved fluctuations, another FFT was performed in the time domain for fixed r, so that the final wave components were fully determined in terms of mode numbers m and the frequency spectrum. In this second FFT, the complex signals were previously multiplied by a Hanning window with a time length of 2 hr, which implies a lower band frequency of about 0.14 mHz. These 2-hr windows were sliding forward in time with an overlapping rate of 15 min. Given the 1-min cadence of the input data, the power spectral densities taken at resonance frequencies and harmonics ($f_d = m\omega_d/2\pi$) were obtained whenever such frequencies were within 0.14–8.33 mHz. Finally, the total power spectral densities found in E_ϕ and B_z fluctuations by considering the resolved m numbers were included in Equations 2–4, and maps of $D_{LL} = D^E_{LL} + D^B_{LL}$ were derived.

D_{LL} calculations were performed for circular orbits at the SM equator so that the radial distances r from the MHD simulations are equivalent to the dipole L shell. Furthermore, dividing the polar grid into 48 uniform slices resulted in mode numbers up to $m = 24$. However, the D_{LL} results to be shown next were derived for $m = 1$–9 because this work is centered on the ULF resonant interaction with high-energy electrons. Using this coverage of m values, we expect to obtain all dominant contributions to D_{LL} from the modeled ULF waves, which correspond to $m < 4$ (e.g., Fei et al. (2006); Z. Li et al. (2016)).

3.2. Radial Diffusion Simulations

To model radiation belt radial diffusion during the two case studies from a realistic initial condition together with dynamic outer boundary conditions, the 1D diffusion equation (Schulz & Lanzerotti, 1974) was numerically solved:

$$\frac{\partial f}{\partial t} = L^{*2}\frac{\partial}{\partial L^*}\left(\frac{D_{LL}}{L^{*2}}\frac{\partial f}{\partial L^*}\right) - \frac{f}{\tau}, \tag{9}$$

where $f(L^*, t)$ represents the phase space density distributions at fixed μ (first) and K (second) adiabatic invariant values, L^* is the Roederer's L, D_{LL} (L^*, t) stands for the input radial diffusion coefficients where the approximation L shell = L^* will be assumed hereafter and f/τ accounts for the loss terms added to the diffusion model for investigation of dropouts.

In all 1D simulations, we have considered:

- The outer boundary defined at $L^* = 6$, along with a time-dependent condition from calibrated PSD values of GOES-15 relative to RBSP-A's PSD observations;

- Initial condition imposed using the first PSD profile available at each selected event, acquired with combined measurements from the Van Allen Probes and GOES-15;
- A static inner boundary condition defined at $L^* = 3$, which was also obtained from the PSD profile of the initial condition;
- The plasmapause location model of O'Brien and Moldwin (2003) built on the *Dst* index running minima as a constraint for electron loss inside the plasmapause;
- Empirical electron lifetimes due to plasmaspheric hiss waves set up inside the plasmapause. The model used is from Orlova et al. (2014) and is parameterized by the *Kp* index;
- The last closed drift shell (LCDS) was calculated with the time-dependent TS04 magnetosphere model (Tsyganenko & Sitnov, 2005) as the constraint for magnetopause shadowing losses; electron lifetimes on the order of its drift period were set beyond this boundary.

Unlike previous work that included the effects of whistler-mode chorus loss in radial diffusion simulations of electron distributions over longer periods (e.g., Mann et al., 2016; Ozeke et al., 2020; Ozeke, Mann, Turner, et al., 2014; Tu et al., 2009), in our simulations we neglected such effects. This was done to focus the analysis of dropout events mainly on the dominant effects from magnetopause shadowing and outward radial diffusion loss, attributed to the global ULF waves simulated with BATS-R-US. Conversely, gradual loss by plasmaspheric hiss waves inside the plasmapause was added in our simulations since it may be important for 1D simulations to reduce the PSD overestimations produced by the inapplicability of some D_{LL} model results within $L^* \sim 3.5$ (e.g., Ozeke, Mann, Murphy, et al. [2014]; Tu et al. [2019]). Although not shown in this paper, RBSP-A and RBSP-B observations of ELF hiss waves (0.1–1 kHz) during the two case studies showed enhanced wave activity for magnetic power spectral densities of 10^{-5} $[nT^2/Hz]$ during the passage of the CIRs and afterward.

3.2.1. Outer Boundary Conditions From Calibrated PSD Observations of GOES-15

PSD observations obtained by the US Geostationary Operational Environmental Satellite GOES-15 in geosynchronous orbit ($r = 6.6\ R_E$) were used to build data-driven outer boundary conditions for the 1D diffusion simulations. The magnetic ephemerides of the GOES spacecraft are not available and so we used the IRBEM-LIB (Boscher et al., 2012) library in MATLAB®. The time-dependent TS04 model implemented in the library was used for shell tracing and computation of K and L^* invariants of the events, at local pitch angles from 30° to 90° with a 10° step.

In turn, PSD data of GOES-15 were converted from differential electron fluxes measured by the Magnetospheric Electron Detector (MAGED). Since the goal is to simulate the dropouts observed by Van Allen Probes, these PSD data from GOES-15 at fixed μ and K invariants were calibrated with those from RBSP-A, as we have found that Probe A normally executed apogees in L^* regions as large as $L^* = 6$. The electron PSD data from RBSP-A or RBSP-B used in this work were converted using MagEIS (Blake et al., 2013) and REPT flux measurements. For context, each Van Allen Probe operated in a highly elliptical orbit ($1.1 \times 5.8\ R_E$) around 10° away from the geographic equator over the course of 2012–2019. As explained in the Supporting Information, calibration factors to correct GOES-15 PSD data against RBSP-A data were later obtained throughout March 2017 for two μ regimes, namely 700 and 1318 MeV/G, with the second invariant set to $K = 0.08\ R_E G^{1/2}$ in both cases. The resulting calibration factors were 1.33 for $\mu = 700$ MeV/G and 5.50 for $\mu = 1318$ MeV/G.

Matching factors between calibrated PSD estimates from GOES-15 and PSD estimates from RBSP-A were calculated for several conjunctions in L^* throughout March 2017, considering $\Delta L^* \leq 0.3\ R_E$. These matching factors are defined as the ratio of the highest to lowest phase space density, both measured at a conjunction site (Reeves et al., 2013). According to the results of Figure S1 (see supporting information), calibrated PSD data of GOES-15 at $\mu = 700$ MeV/G is the most accurate with PSD measurements by RBSP-A. Thus, we chose to run all 1D diffusion simulations only for $\mu = 700$ MeV/G, using the calibrated PSD data from GOES-15 in this lower μ regime for the outer boundary conditions.

Also, Figure S2 of the supplementary information shows concurrent PSD observations at $\mu = 700$ MeV/G and $K = 0.08\ R_E G^{1/2}$ from RBSP-A, RBSP-B, and GOES-15 during (a) case study 1 and (b) case study 2, for calibrated PSD data in geosynchronous orbit. Gaps in the GOES-15 PSD data refer to gaps in L^* associated with main phase incursions of the last closed drift shell, as will be identified later in Figure 2. It can be seen in Figure S2 that the several instances of L^*-conjunctions between GOES-15 and the Van Allen Probes indicate that the calibrated PSD estimates from GOES-15 well correspond to RBSP-A/RBSP-B observations (e.g., the

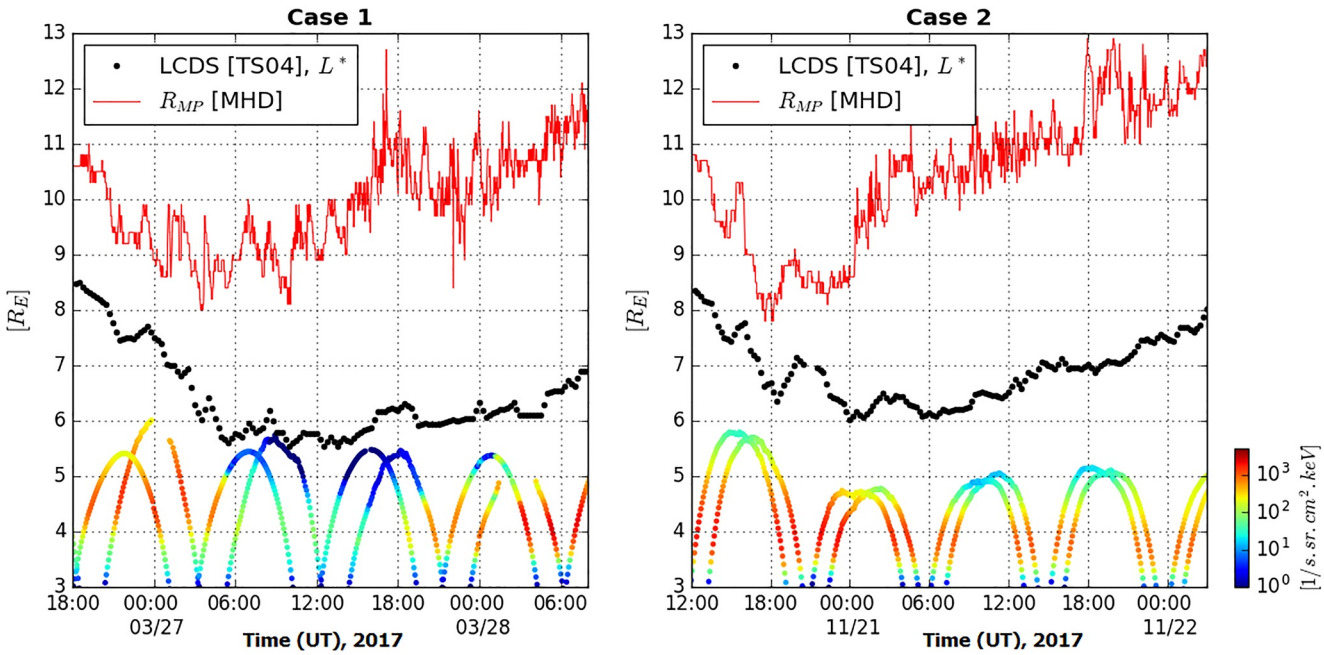

Figure 2. Comparisons of the time evolution of the magnetopause location (R_{MP}) simulated with magnetohydrodynamic and the last closed drift shell (LCDS) modeled with TS04 to assess the extent of the losses by magnetopause shadowing during the flux dropouts of Case 1 (left) and Case 2 (right). The Van Allen Probes (REPT) electron fluxes at 1.8 MeV and 90° pitch angle shown for both cases below the R_{MP} and LCDS results are sorted by UT time and L^* derived with the TS04 model.

conjunction with RBSP-A just after 12 UT on 26 March at $L^* \sim 6$, and in the panel below on 20 November also just after 12 UT). Furthermore, the timing and intensity of PSD variations observed by the three spacecraft are in good agreement across L^* shells.

To build the dynamic outer boundary conditions in each 1D simulation, we assumed that the calibrated PSD data from GOES-15 were obtained at $L^* = 6$. In fact, the results of L^* in Figure S2 of Supporting Information S1 show that the L^* values calculated with the TS04 model in geosynchronous orbit decrease with storm time, going from $L^* \sim 6$ to $L^* \sim 5$ in Case 1 (panel a), and to $L^* \sim 5.5$ in Case 2 (panel b). It should be noted that the same assumption for the outer boundary condition was also made in previous works (e.g., Z. Li et al., 2014).

4. Results

4.1. Magnetopause Shadowing

Figure 2 shows comparisons of the time evolution of the magnetopause standoff distance (R_{MP}) simulated by BATS-R-US (in red) and of the last closed drift shell modeled with TS04 (in black) for the case studies. To calculate the R_{MP} curve using global MHD simulations, we inspected the instantaneous location of the maximum peak in the total current density profile along the SM x-axis, which was then taken as the distance from the magnetopause nose to the center of the Earth (similar to Medeiros et al. [2019]). The figure also shows 5-min averaged electron fluxes at 1.8 MeV and 90° pitch angle in the outer belt as a function of L^*, calculated with the TS04 model.

It can be seen from the results of R_{MP} that in both cases the dayside magnetopause was compressed to ~8 R_E along the storm-time intervals, according to the MHD simulations. This indicates that no important distinction can be made, in terms of the extent of magnetopause losses for the two dropouts analyzed. On the other hand, LCDs analysis clearly shows that Case 1 was more affected by LCDS incursions into low L^* shells and, consequently, by magnetopause shadowing. Specifically, LCDS is observed to go down to $L^* \sim 5.5$ in Case 1, while not going beyond $L^* = 6$ in Case 2. In addition, the observations of strong flux dropout in Case 1 on 27 March are seen concurrently with the LCDS inward incursions, while in Case 2 the observations of the mild flux dropout spanning $L^* \geq 4.5$ through 21 November (after 6 UT) are seen following such LCDS incursions. In summary,

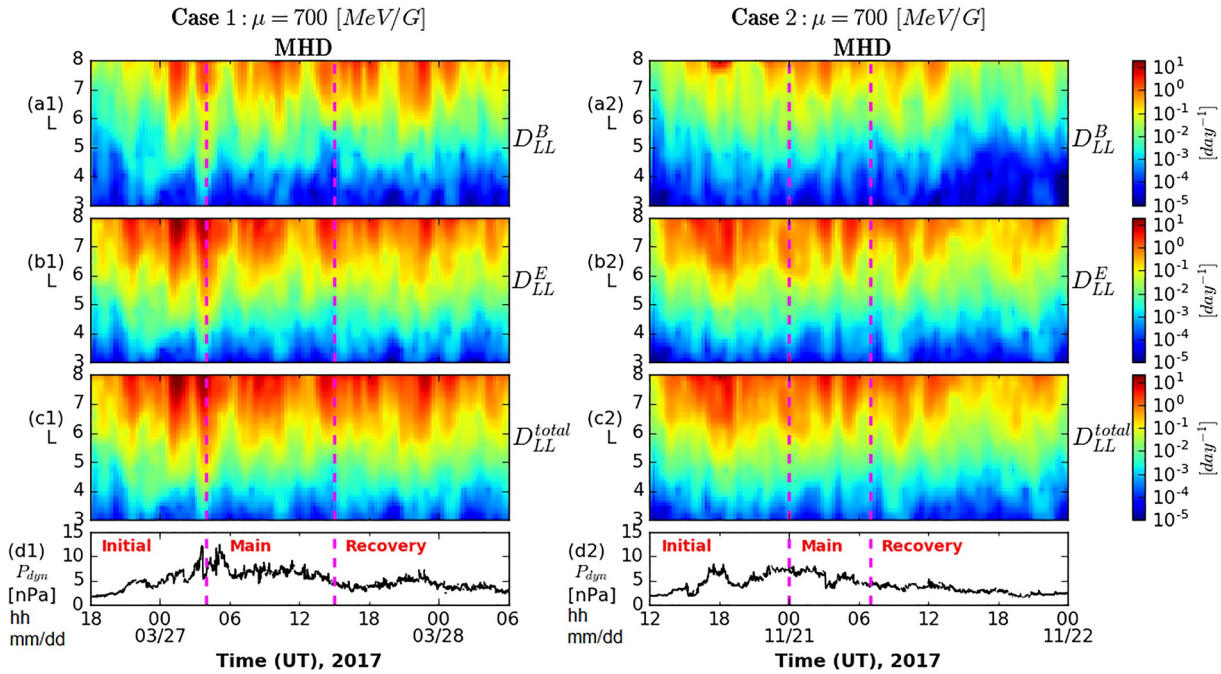

Figure 3. Maps of event-specific radial diffusion coefficients from magnetohydrodynamic computed for $\mu = 700$ MeV/G, as a function of the UT time and dipole L shell. D_{LL}^{B} and D_{LL}^{E} represent the radial diffusion rates from the electron drift-resonance with ULF waves in the simulated SM-B_z and SM-E_ϕ fields. D_{LL}^{total} corresponds to the total diffusion rates given by the sum of D_{LL}^{B} and D_{LL}^{E}. The pink dashed lines in these maps depict the storm main phase interval. Panels d1 and d2 contain the solar wind dynamic pressure curves with the indication of each storm phase interval. The intervals for analysis shown for both events start from beginning of the initial phase up to the early recovery phase.

these LCDS results demonstrate that magnetopause shadowing could be more operative during Case 1 and play a greater role for its flux dropout.

4.2. Event-Specific D_{LL} Coefficients

Figure 3 shows storm-time radial diffusion coefficient maps for the two case studies derived from the global MHD fields using Equations 2–4. The different panels present the magnetic and electric counterparts of D_{LL}[MHD], its total rates, and the dynamic pressure of the solar wind. These D_{LL} results were obtained for $\mu = 700$ MeV/G, which corresponds to 1 MeV electrons at $L \sim 4.7$ in a geomagnetic dipole and assuming $K = 0$ $R_E G^{1/2}$ for the second invariant. The various maps show results from D_{LL} up to $L = 8$, as it was shown in Figure 2 that the magnetopause is compressed to these altitudes over storm time.

It is observed that D_{LL} rates increase largely with L and that D_{LL}^{E} is the dominant component of D_{LL}, as already been widely reported in the literature (e.g., Huang et al., 2010; Z. Li et al., 2016; Ozeke, Mann, Murphy, et al., 2014; Tu et al. [2012]). Furthermore, comparing panels a1 and a2 of Figure 3, it can be seen that D_{LL}^{B} is higher for Case 1 through storm time in $L > 5$ than for Case 2. As for the D_{LL}^{E}, panels b1 and b2 indicate that this comparison is not so straightforward, despite the D_{LL}^{E} from Case 1 reaching intensities from over 10/day at $L \geq 7$ to 1/day at $L = 5$ in the late initial phase of the storm. Also, the high intensity (1/day) diffusion rates from D_{LL}^{E} are more sustained in Case 1 than in Case 2 throughout the intervals shown, with the latter also weakening drastically during the recovery phase.

Similar results are also found for total D_{LL}[MHD]. Figure 3 (panel c1) shows that, in Case 1, the total D_{LL}[MHD] peaks twice down to $L = 5$ in response to pressure pulses inside the CIRs, as can be seen in panel d1 after 0 UT on 27 March. Also in Figure 3 (panel c1), high-intensity diffusion rates outside $L = 6$ are sustained until the early recovery phase. Panel c2 shows that a less intense D_{LL} peak is induced down to $L = 5.5$ for Case 2 by the dynamic pressure pulse at ~18 UT on 20 November. And again, the high-intensity diffusion rates observed outside $L = 6$ weaken during the recovery phase. All these observations for storm-time D_{LL} from the global MHD simulations agree, for example, with earlier observational work by Sandhu et al. (2021). Using the Van Allen Probes database,

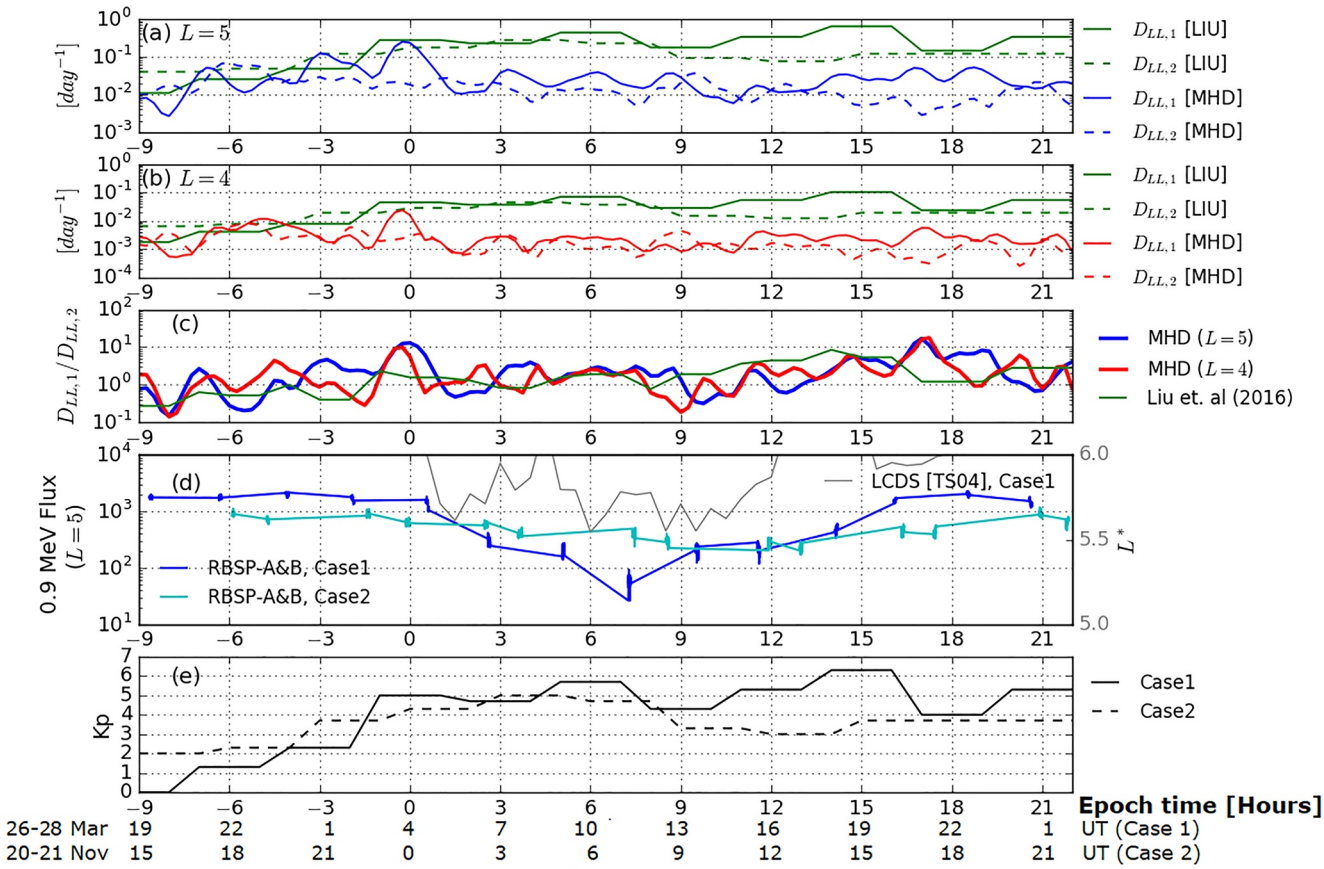

Figure 4. Superposed epoch comparisons of simulated and empirical D_{LL} results from Case 1 ($D_{LL,1}$[MHD] and $D_{LL,1}$[LIU]) with corresponding results from Case 2 ($D_{LL,2}$[MHD] and $D_{LL,2}$[LIU]) at (a) dipole $L = 5$ and (b) dipole $L = 4$. The x-axis of each panel refers to epoch time in units of hours, where the zero epoch time (Ep = 0 hr) was defined by the start of the main phase of the events. Panel (c): direct ratios obtained for $D_{LL,1}$[MHD]/$D_{LL,2}$[MHD] at $L = 4$ (red curve) and $L = 5$ (blue curve), and obtained for $D_{LL,1}$[LIU]/$D_{LL,2}$[LIU] which is constant with L (green curve). Panel (d): time evolution of MagEIS electron fluxes at 0.9 MeV for 90° pitch angles, using both Van Allen Probes throughout case studies 1 and 2 (blue lines). The result of the last closed drift shell in Case 1 is overplotted in gray. Panel (e): time evolution of *Kp* indices driving the Liu et al.'s empirical radial diffusion rate estimates during case studies 1 and 2. The UT time information corresponding to each case study during the 31-hr interval analyzed is also indicated below panel (e).

these authors also showed that the total radial diffusion coefficients enhance mostly from the late initial to the main storm phase, in association with enhancements in the magnetic and electric components of D_{LL}. Furthermore, they showed that D_{LL} rates tend to decrease toward the end of the storm. However, we observed for Case 2 that the D_{LL} weakening took place already within the early recovery phase. Moreover, our results indicate that solar wind driving, through the dynamic pressure pulses identified for cases 1 and 2, exerts an important role in generating D_{LL} enhancements in low L shells during storm time.

4.3. D_{LL} Comparisons

Figure 4 displays superposed epoch analysis of D_{LL}[MHD] for fixed L shells. The graphs show the behavior of event-specific diffusion rates in the region where flux dropouts were probed by RBSP-A and RBSP-B (i.e., $L < 6$). A comparison of this behavior between the two case studies is also presented, with the Epoch time zero defined by the main phase start in both cases. The main phase started at 4 UT on 27 March for Case 1 and at 0 UT on 21 November for Case 2. The figure also contains comparisons with empirical radial diffusion coefficients calculated with the model of Liu et al. (2016), defined as:

$$D_{LL}^{E}[LIU] = 1.115 \cdot 10^{-6} \cdot 10^{(0.281 \times Kp)} \cdot L^{8.184} \cdot \mu^{-0.608}. \quad (10)$$

This model for D_{LL}^{E} derives *Kp*-based electric radial diffusion coefficients and was obtained from 7-year (2008 − 2014) measurements of quasi-azimuthal electric field power spectral densities by THEMIS-D (Time History of Events and Macroscale Interactions during Substorms). Unlike D_{LL}[MHD] which includes D_{LL}^{B} contribution and uses mode numbers $m \leq 9$, single mode $m = 1$ was assumed for D_{LL}[LIU]. It was chosen for comparison with D_{LL}[MHD] results because it explicitly expresses the dependence on μ.

In Figures 4a and 4b, it can be seen that the D_{LL}[MHD] peak of Case 1 (solid blue/red lines) at Epoch time zero (Ep = 0 hr) stands out when compared to the D_{LL}[MHD] results of Case 2 (dashed blue/red lines) at both $L = 5$ and $L = 4$. This demonstrates that the effect of the second D_{LL} enhancement identified previously for Case 1 in Figure 3 (panel c1) actually reaches $L = 4$. From 1 < Ep < 15 hr, D_{LL}[MHD] of Case 1 is mostly comparable to D_{LL}[MHD] of Case 2 in both *L* shells. At Ep = 15 hr, D_{LL}[MHD] of Case 1 slightly increases, while D_{LL}[MHD] of Case 2 decreases slightly in both *L* shells. It is also clear that Case 1 D_{LL}[MHD] exhibits more variability across the storm.

In these same figures, the results for D_{LL}[LIU] from Case 1 (solid green lines) and from Case 2 (dashed green lines) are also plotted. We find D_{LL}[LIU] results are comparable to those from D_{LL}[MHD], at both *L* shells, only in the initial phase (i.e., up to Ep = 0 hr for Case 1). As the *Kp* index in Figure 4e shows similar moderate values of >3 approaching Ep = 0 hr in both events, D_{LL}[LIU] is able to reproduce the highest D_{LL} peak in Case 1, but over reproduces the D_{LL} peak at Ep = 0 hr in Case 2. Subsequently, as shown in Figures 4a–4b, D_{LL}[LIU] becomes an order of magnitude larger than the respective responses of D_{LL}[MHD] for the two cases, regardless of *L*. On the other hand, D_{LL}[LIU] is roughly comparable between the two cases throughout the initial and main phases. As the recovery phase starts for Case 2 at Ep = 7 hr, the difference in empirical radial diffusion rates of the events becomes apparent, as seen after Ep = 9 hr.

To better illustrate the different levels of D_{LL} between the two cases, Figure 4c shows the ratio between D_{LL} curves from panels 4a and 4b, with the results of the ratio for $L = 5$ between Case 1 D_{LL}[MHD] curve and Case 2 D_{LL}[MHD] curve in blue, the same analysis for $L = 4$ in red, and that obtained for D_{LL}[LIU] in green. It should be noted, based on Equation 10, that the D_{LL} ratios of Liu et al.'s model between two cases are constant with *L*. Figure 4d shows the electron fluxes at $L = 5$ derived from measurements by both Van Allen Probes, at the kinetic energy corresponding to $\mu = 700$ MeV/G (i.e., 0.9 MeV). It is observed that the fast flux dropout in Case 1 is ∼2 orders of magnitude, while in Case 2 the dropout is less than an order of magnitude. Overplotted is the result of the last closed drift shell of Case 1 in Figure 2 to indicate how the radial diffusion and magnetopause shadowing processes were combined during the strong flux dropout. It can be seen in Figure 4c that the D_{LL} ratios between the two cases are generally greater than one during storm time, as obtained for both *L* shells with the empirical model and MHD. Thus, D_{LL} rates in Case 1 were overall higher than in Case 2 over the storm phases. Specifically, the higher D_{LL} of Ep = 0 hr in Case 1 compared to Case 2, with ratios up to 10, together with a reduced level of diffusion in the early main phase indicated by ratios ∼3, imposed an enhanced level of outward radial diffusion for radiation belt electrons in Case 1 compared to Case 2. Furthermore, this enhanced diffusion rate during the main phase operated simultaneously with the magnetopause shadowing (see the LCDS curve in panel d) both of which could contribute to a major flux dropout.

Regarding the *L* dependence of D_{LL} ratios from MHD between the two case studies, Figure 5a shows a superposed epoch map of these ratios. It is observed that the Case 1 D_{LL}[MHD] was higher than that of Case 2 over a wide range of *L* shells in its late initial phase (just before Ep = 0 hr), around the main phase and especially during its recovery phase (after Ep = 11 hr). The largest ratios above 20 appear mostly outside of $L = 7$. Inside $L = 6$, which is where the 1D simulation domain was defined, the ratios of ∼10 related to the second D_{LL} peak at Ep = 0 hr cover the entire range $3 < L \leq 5.5$. After Ep = 0 hr, when the flux dropouts are ongoing, the ratios decrease to <5 within the same range of *L*, and only indicate larger factors in Case 1 D_{LL}[MHD] in $L > 5.5$. The ratios in the recovery phase can be higher than 20, especially at Ep = 17 hr when a second instance of strong D_{LL} enhancement for Case 1 in relation to Case 2 is found at low *L*. This happens in association with flux recovery in Case 1. The results of the large ratios at Ep = 0 hr reinforce the role of enhanced radial diffusion dynamics acting throughout the outer belt region during the flux dropout of Case 1. It is also useful to show the difference between empirical- and MHD-D_{LL} on an L-sort map. This is plotted in Figures 5b–5c for both cases, where D_{LL}[LIU] is seen to be ∼0.5–2 orders of magnitude higher than the corresponding D_{LL}[MHD] through storm time, especially after the main phase and at inner *L* shells.

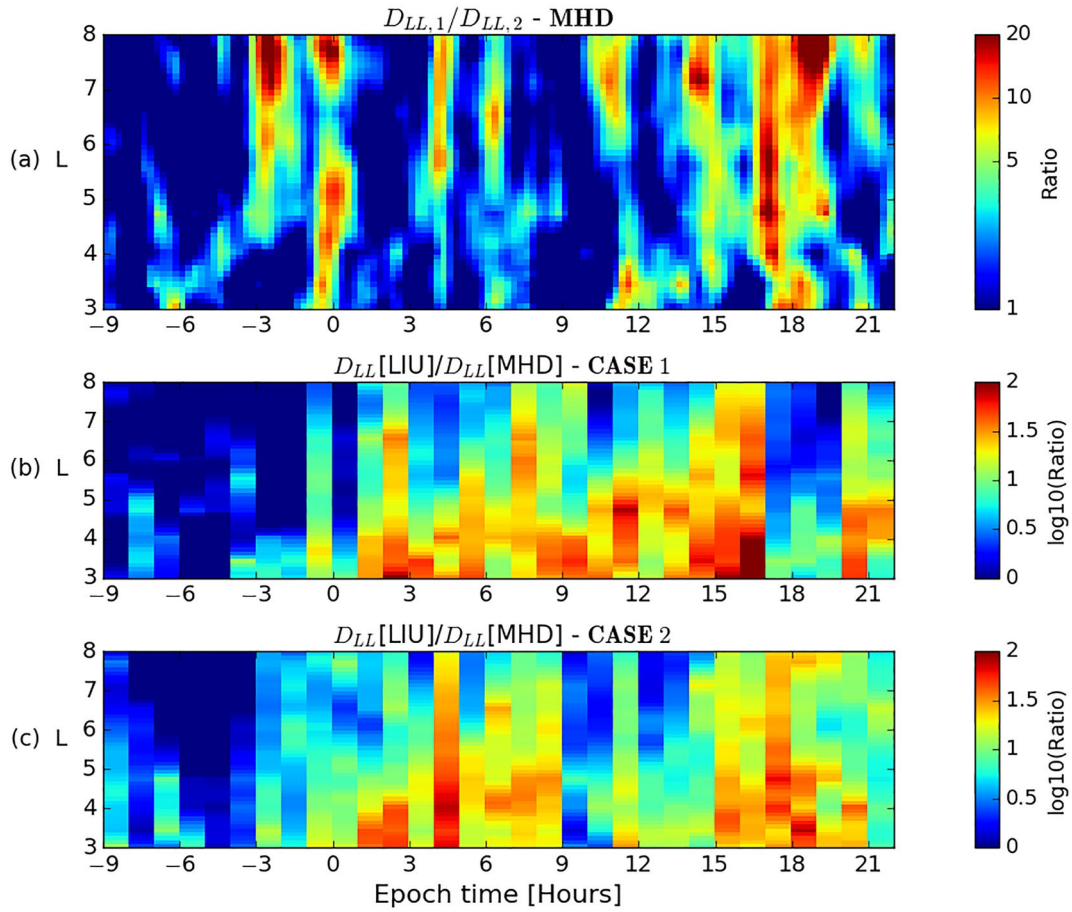

Figure 5. (a) Map of difference ratios in total D_{LL} defined between D_{LL}[MHD] from Case 1 and D_{LL}[MHD] from Case 2, observed across L shells and the superposed epoch times. The epoch time zero (Ep = 0 hr) has been defined by the main phase start of the events. (b)–(c) Similar analysis, but for the difference ratios defined between results of empirical D_{LL}[LIU] and corresponding results of D_{LL}[MHD] during (b) Case 1 and (c) Case 2.

4.4. MHD Validations

To validate the MHD-simulated global electric and magnetic fields used in the D_{LL} calculation, short intervals were selected from the MHD simulations for which RBSP-B observations of those fields were available for comparison. It was chosen not to show validations for all simulation intervals since the electric field data of Case 1 is very noisy during part of the storm time. The in-situ electric and magnetic fields used were taken from the Electric Field and Waves (EFW; Wygant et al. [2013]) and Magnetic Field Instrument Suite and Integrated Sciences (EMFISIS; Kletzing et al. [2013]) aboard the RBSP-B. Figure 6 shows the probe orbital location in the SM equatorial plane and in the X-Z meridional plane in these selected intervals for the two cases studied. Both intervals refer to ULF wave observations during the storm's main phase.

Figure 7 presents the MHD validations obtained for Case 2 from 23:30 UT on 20 November to 3 UT on 21 November 2017. Figures 7a–7f sequentially show comparisons along the RBSP-B orbit of simulated versus measured dayside ULF fluctuations in SM-B_z and SM-E_ϕ, and the respective wave power spectra. These ULF fluctuations were extracted by detrending the measured and simulated fields with a 15-min running window to remove the background fields. The field perturbations obtained from the observed fields were smoothed with a 1-min running window and the power spectral densities were estimated using Fourier transform over a rolling one-hour window. Figure 7g indicates that in this short time interval of Case 2, the RBSP-B was located between $L = 4.5$ and $L = 6$ during an inbound pass through the prenoon sector.

It can be seen in Figures 7a–7c that the MHD coupled model works well to reproduce the wave power in B_z on the dayside. Meanwhile, it is shown in Figure 7d that the irregular ULF waveforms in the measured E_ϕ signals

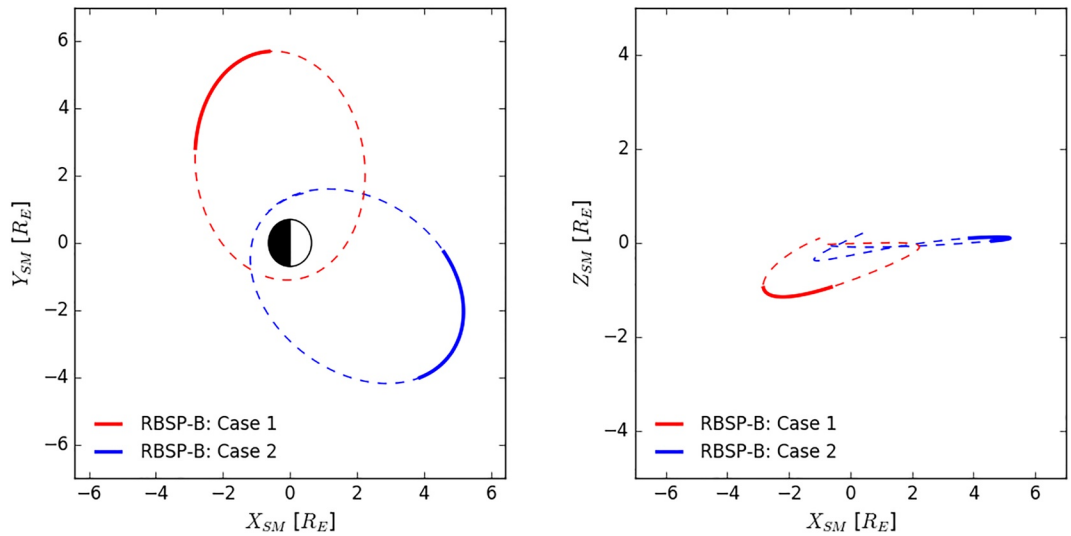

Figure 6. Locations of Van Allen Probe B in the SM equatorial plane (left) and on the X-Z plane (right), over the short intervals of the magnetohydrodynamic simulations in Case 1 and Case 2. This probe was moving eastward while it was in operation from 2012 to 2019. The dashed lines in these plots show the remaining parts of the complete RBSP-B's orbit during each case study.

are only partially reproduced by the MHD model. Thus, the simulated wave power can be generally comparable to the observations, although localized wave packets at frequencies >2.5 mHz, as seen just after 23:30 UT on 20 November, are not all reproduced by the MHD simulation (see panels 7e and 7f).

The MHD validations for Case 1 of nightside ULF fluctuations are shown in Figure 8, in the same format as Figure 7. The time interval considered is from 06:30 UT to 09:30 on 27 March and, during this period, the RBSP-B was also located between $L = 4.5$ and $L = 6$ during a pass inbound through the post-dusk sector (see Figure 8g). As for B_z, the MHD model mainly reproduces the low frequencies of the ULF signals observed on the night side, so the wave power of higher frequencies is significantly underestimated. Likewise, the model results for E_ϕ indicate that there is an underestimation of the ULF wave power, especially at high frequencies.

The above-described MHD validations indicate that ULF fluctuations and wave power in B_z and E_ϕ are generally comparable to the observations available for the dayside, while the results for the nightside are underestimated. These underestimations on the nightside in the post-dusk sector are interpreted as due to the time and maximum grid resolutions (1 min/0.25 R_E). As a result, MHD simulations were not able to handle fast and more localized Pc5 phenomena driven by substorm activity. Moreover, to explain why some high frequency wave packets in the E_ϕ power spectra were not reproduced on the dayside (Figure 7), it has been already suggested in other studies that the convection E_ϕ field component calculated by the MHD simulations may be limited to capturing small-scale ULF wave activity with correspondingly large mode numbers (e.g., L.-F. Li et al. [2020]). It is known that narrowband ULF waves are likely generated by internal sources, that is, resulting from drift-bounce resonances with ring current ions (Sandhu et al. [2021] and references therein). According to Jauer et al. (2019), solving the drift physics of the bulk flow through the inner magnetosphere, as in our MHD simulations by CIMI, is critical to determining the local power distribution of these high-frequency E_ϕ ULF waves.

4.4.1. Average Power Analysis for Scaling MHD-D_{LL}

The superposed epoch comparisons between D_{LL}[MHD] and D_{LL}[LIU] for fixed L shells shown earlier in Figure 4 indicated that MHD-D_{LL} can be more than an order of magnitude smaller than the empirical estimates of D^E_{LL} modeled using Liu et al. (2016). Additionally, through comparisons with RBSP-B observations, it was concluded that the MHD simulations underestimated the ULF wave power for both E_ϕ and B_z fluctuations on the night-side. These observations indicate that scaling of the MHD-D_{LL} results by some factor is necessary for these event-specific diffusion rates to become more realistic for 1D diffusion simulations.

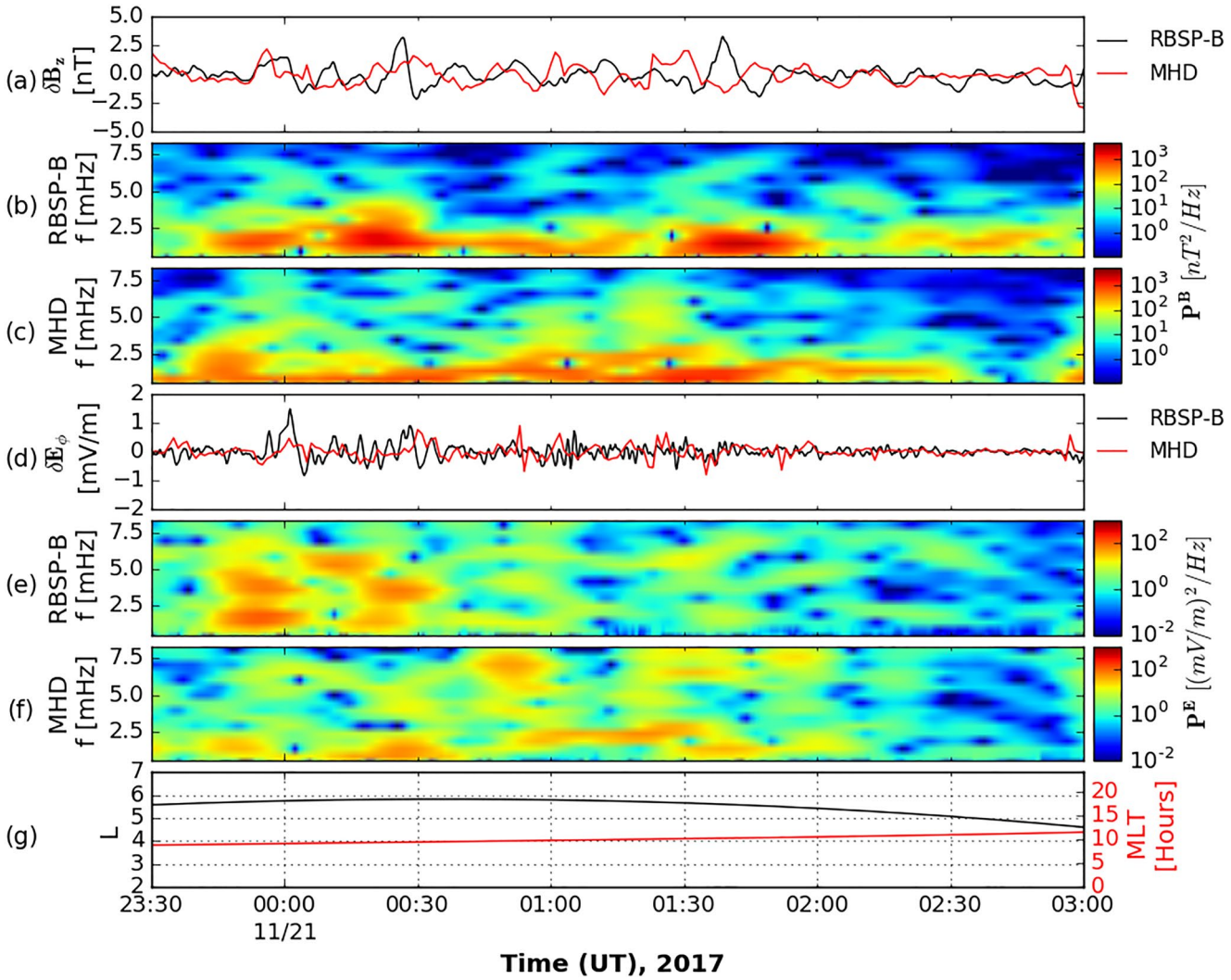

Figure 7. Magnetohydrodynamic validations for case study 2 on the dayside using Van Allen Probe B, during 20–21 November 2017. Panel (a): comparisons of the measured (black) and modeled (red) field perturbations in SM-B_z. Panels (b)–(c): respective spectrograms of measured and modeled B_z field perturbations. Panel (d): comparisons of the measured (black) and modeled (red) field perturbations in SM-E_ϕ. Panels (e)–(f): respective spectrograms of measured and modeled E_ϕ field perturbations. Panel (g): L and MLT regions covered by Radiation Belt Storm Probes-B during this interval.

The scale factors for MHD-D_{LL} were derived here based on the ULF wave power comparisons in Figures 7 and 8. They were defined as the mean value of the ratio between the measured and simulated power spectra, averaged over the ULF frequency range 1–8.33 mHz and over time. As D_{LL}^E is the dominant contribution to total D_{LL}[MHD], these factors were calculated considering only the E_ϕ wave spectra in both the case studies. It turns out the scale factors to correct MHD-D_{LL} are 2.93 for Case 1 and 1.37 for Case 2. Figure 9 presents the results of this analysis, with the simulated MHD, measured, and scaled MHD shown in blue, green, and red, respectively. It can be seen in Figure 9a that during the short time interval of Case 2, the MHD average power is comparable to the RBSP-B average power on the dayside, with an average ratio of 1.37. In turn, in the time interval of Case 1, the MHD average power is much more underestimated on the nightside with an average ratio of 2.93 (see Figure 9b), similar to report for the MHD validations.

4.5. 1D Simulation Results

In order to model the different dropout dynamics observed in the two case studies, radial diffusion simulations were performed using outer boundary conditions from the calibrated PSD values of the GOES-15 and the scaled MHD-D_{LL}. Radial diffusion runs were also performed using the non-scaled results of D_{LL}[MHD] and

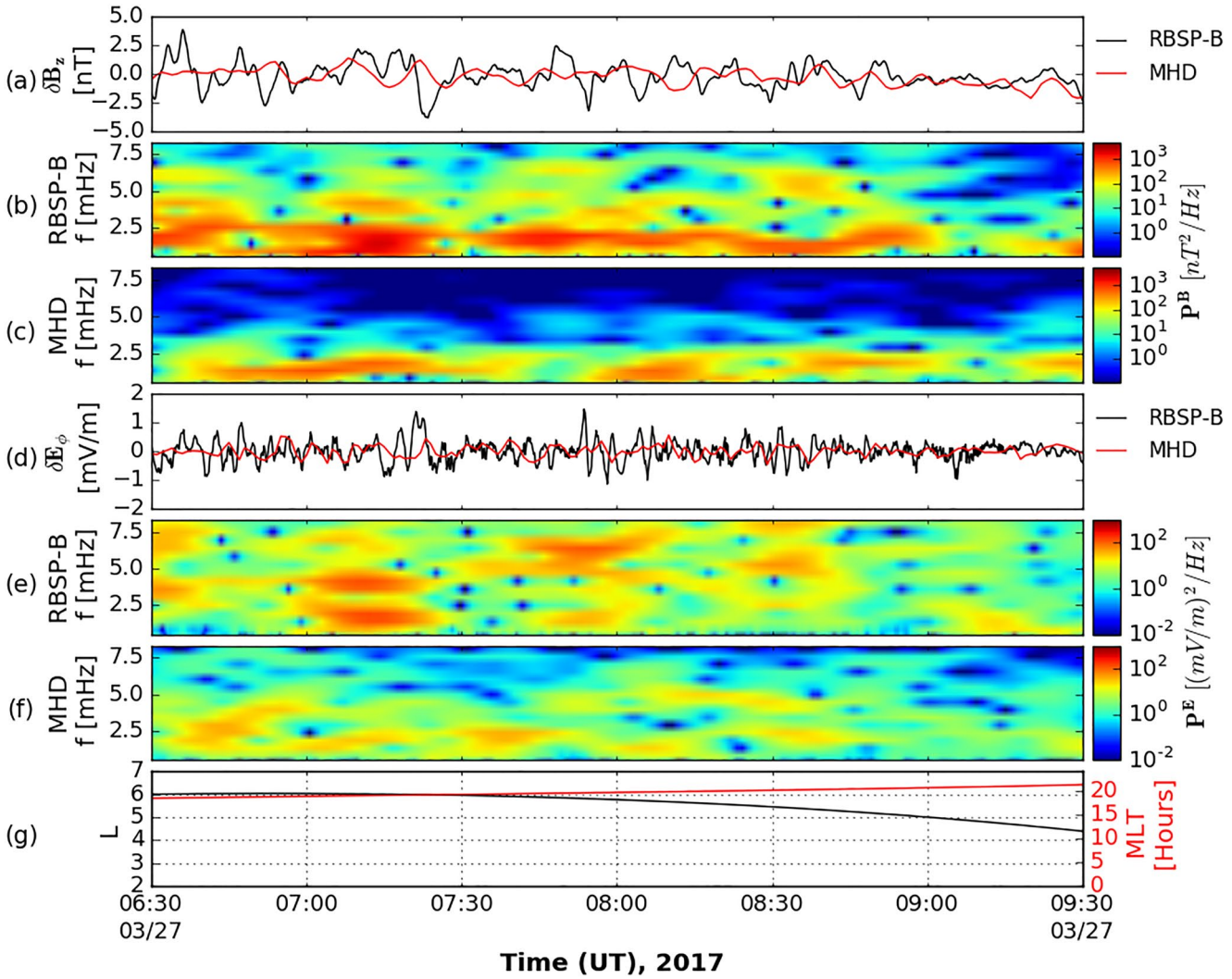

Figure 8. Same as Figure 7, but with the magnetohydrodynamic validations for case study 1 on the night side, on 27 March 2017.

the empirical D_{LL}[LIU] for comparison. Regarding the loss terms, electron lifetimes due to hiss loss were set inside the plasmapause for the simulations, while electron lifetimes due to magnetopause shadowing loss were imposed outside the last closed drift shell when this limit was below the outer boundary located at $L^* = 6$. Thus, the magnetopause shadowing loss was set in the 1D simulations only for Case 1, following the results found in Figure 2. The simulations were solved for relativistic electrons with $\mu = 700$ MeV/G and $K = 0.08\ R_E G^{1/2}$.

Figure 10 shows PSD observations versus PSD results from 1D diffusion simulations for cases 1 (left panels) and 2 (right panels). Panels a1 and b1 contain the PSD observations by the Van Allen Probes, panels a2 and b2 show the maps with simulation results using scaled-D_{LL}[MHD], and panels a3 and b3 show the maps obtained using D_{LL}[LIU]. The locations of the last closed drift shell below $L^* = 6$ are overplotted for Case 1 in panels a1–a3. The results of the 1D simulation at fixed $L^* = 4.9 \pm 0.05$ and $L^* = 4.3 \pm 0.05$ are shown in panels a4–b4 and a5–b5, respectively, for all D_{LL} coefficients considered, that is, non-scaled-D_{LL}[MHD] (dashed red lines), scaled-D_{LL}[MHD] (solid red lines) and D_{LL}[LIU] (solid blue lines). In addition, the level of uncertainty in modeled PSD associated with the uncertainty in D_{LL}[MHD] scaled by mean factors of 2.93 (Case 1) and 1.37 (Case 2) is also displayed by the gray area around the solid red curves generated using the mean scaling factors. Specifically, to calculate this uncertainty range in PSD, each diffusion simulation was run with D_{LL}[MHD] scaled by factors equivalent to the minimum and maximum ratios between the averaged RBSP-B power and averaged MHD wave power shown in Figure 9 (green and blue curves respectively). In all these panels of Figure 10, the measured and simulated PSD results were plotted against L^* and superposed epoch times, with time zero referring to the

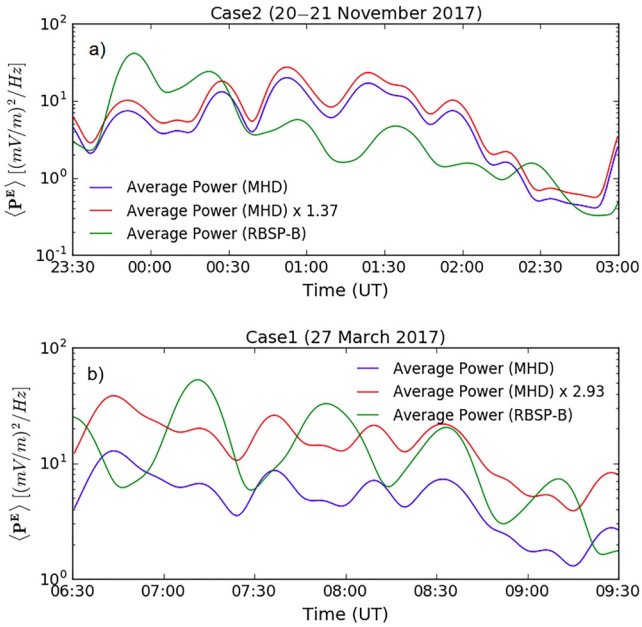

Figure 9. Time-varying averaged power spectral density over the ULF frequency range 1–8.33 mHz, during the short intervals selected for magnetohydrodynamic (MHD) validations of (a) Case 2 and (b) Case 1. Blue lines stand for the average ultra low frequency power simulated with MHD along the Radiation Belt Storm Probes (RBSP)-B's orbits, green lines show results from the measured average power by RBSP-B through these paths, and the red lines show the MHD average power scaled by a factor derived from the mean value of the direct ratio between the latter two power curves, that is: Average Power (RBSP-B)/Average Power (MHD). The scale factors found are equal to 2.93 for Case 1 and 1.37 for Case 2.

onset of the storm main phases. Thus, the analyzed interval is the same as in Figures 4 and 5. The corresponding UT time of each interval is also shown in panels a5 and b5.

It is observed in panels a1 and b1 of Figure 10 that the PSD data by the Van Allen Probes also demonstrate a stronger and deeper dropout of relativistic electrons in Case 1 than Case 2. In general, it can be seen in panels a2–a3 that 1D simulations using scaled-D_{LL}[MHD] or D_{LL}[LIU] generated the main phase dropout during Case 1, but the run with D_{LL}[LIU] better captures the deep losses to $L^* = 4$ as observed by Van Allen Probes. For the Case 2 dropout, the results of panels b2–b3 indicate that the run with D_{LL}[LIU] generated the outward diffusion loss down to $L^* < 4.5$, thus overestimating the loss in this region since the observed losses were only at higher L^* regions. In turn, the scaled-D_{LL}[MHD] resolved the main phase dropout down to $L^* \sim 5$ for Case 2, and modeled PSD is comparable with observations within $4 \leq L^* \leq 4.5$. Furthermore, PSD recovery after the dropout was also simulated by the model using event-specific D_{LL} inputs, starting after Ep = 12 hr for Case 1 and after Ep = 16 hr for Case 2. These simulated PSD recoveries are results of inward radial diffusion from an external source in a geosynchronous orbit (outer boundary). Overall, the model captures some of the PSD recoveries, but not as fast and deep in L^* as in the observations, possibly due to the lack of local heating in the model. As a local heating and other acceleration mechanisms are outside the scope of this study, no further attempts were made to interpret the results related to the flux and PSD recovery during the case studies.

It can be concluded that the 1D simulations worked well to model the timing and corresponding intensity of the large-scale dynamics of the radiation belt electrons through the storm time, although PSD overestimations at $L^* \leq 3.5$ are noticed in all simulation results of panels a2–a3 and b2–b3 in Figure 10. This is caused by the inapplicability of D_{LL} models in this region (e.g., Ozeke, Mann, Murphy, et al. (2014)) and is also indicative that the inclusion of hiss loss inside the plasmapause was not sufficient to compensate for the large inward radial diffusion of electrons imposed by scaled-D_{LL}[MHD] and D_{LL}[LIU] at $L^* \leq 3.5$.

In comparing PSD observations of both cases at fixed L^* in Figure 10 (black and green symbols in panels a4 and b4), it is found that the PSD dropout in large L^* shells ($L^* = 4.9$) is an order of magnitude for both events. This contrasts with the result of the 0.9 MeV flux decay at the dipole $L = 5$ (Figure 4d), where it was found that the dropout of Case 1 was much stronger than that of Case 2. This higher dropout was due to adiabatic loss effects of 0.9 MeV electron fluxes, which are removed from PSD calculation (e.g., Chen et al. (2006)). This difference in dropout intensity between the two events is observed by both Van Allen Probes at lower L^* as shown in panels a5 and b5 of Figure 10. At $L^* = 4.3$, while the PSD measured in Case 1 drops by an order of magnitude, the PSD decay in Case 2 is less than an order.

Panels a4–a5 and b4–b5 in Figure 10 also show that, on average, the diffusion simulations with scaled event-specific D_{LL} (solid red lines) captured the levels of electron dropouts in the larger L^* shell for both cases as well as the less abrupt loss at $L^* = 4.3$ in Case 2, but they were not able to reproduce the fast dropout of Case 1 deep down to the lower L^* shells. It is only when the D_{LL}[MHD] was scaled to the maximum value (lower limit of the gray area) that the fast dropout at low L^* could be reproduced. These PSD simulation results demonstrate that outward radial diffusion, as simulated with scaled event-specific radial diffusion coefficients, played a significant role in these main phase dropouts and, on average, almost entirely explains the dropout occurrence in Case 2, but only partially in Case 1.

On the other hand, scaling D_{LL}[MHD] with in situ ULF wave power observations improved mostly the model results for the dropout of Case 1, at both low and high L^* regions (comparing the dashed and solid red curves in panels a4–a5 of Figure 10). Conversely, Case 2 acquired very similar radial diffusion responses given by

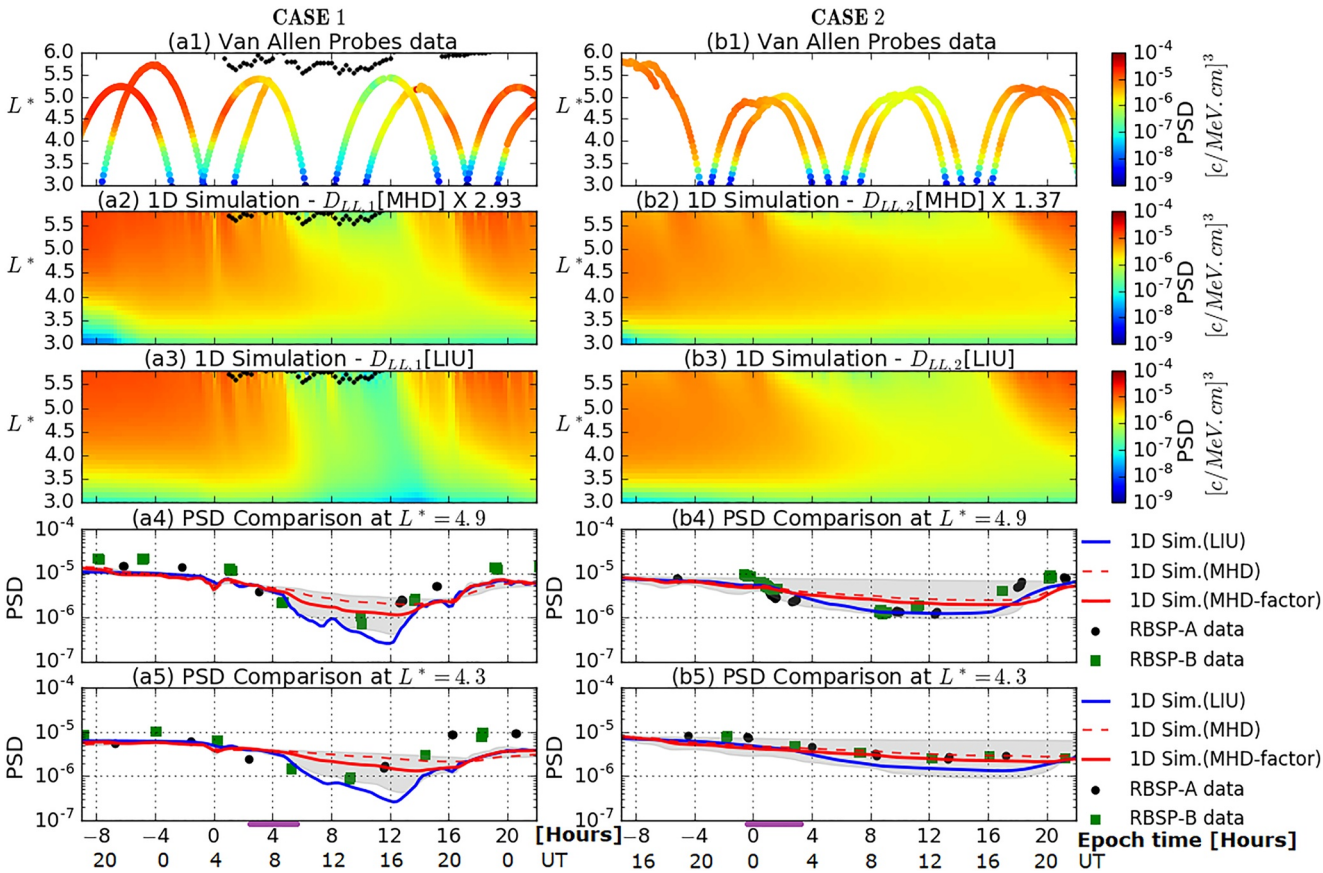

Figure 10. Comparisons of 1D simulation results in PSD (phase space density) versus Van Allen Probes observations both at $\mu = 700$ MeV/G and $K = 0.08\ R_E G^{1/2}$, as a function of L^* and epoch/UT times in units of hours, (left) from 26 to 28 March for case study 1 and (right) from 20 to 21 November for case study 2. The epoch time 0 (Ep = 0 hr) was defined by the main phase start of the events, which is at 4 UT of 27 March for Case 1, and 0 UT on 21 November for Case 2. (Top to bottom) Van Allen Probes PSD observations, simulation results throughout the outer belt using scaled-D_{LL}[MHD] as input, and using D_{LL}[LIU] (panels a1–a3 have the last closed drift shell below $L^* = 6$ represented by the black dotted curve for Case 1), phase space density (PSD) comparisons of simulation results from all D_{LL} inputs (non-scaled-MHD, scaled-magnetohydrodynamic (MHD), and from Liu et al., 2016) with Van Allen Probes observations at a fixed higher L^* location; the same analysis but for a fixed lower L^* value. In these last two panels from top to bottom, the level of uncertainty in modeled PSD using scaled-D_{LL}[MHD] is shown by the gray area for the entire time span of the diffusion simulations. The magenta bar on the bottom-most panels indicates the event's time interval of the MHD-D_{LL} scaling.

Table 1
Normalized Root Mean Square Errors (nRMSE) for Comparing PSD Estimates During the Analyzed Dropout Events Using Three Different D_{LL} Input Coefficients and in Two Different L^*

	Case 1		Case 2	
	$L^* = 4.9$	$L^* = 4.3$	$L^* = 4.9$	$L^* = 4.3$
D_{LL} input	$n = 7$	$n = 5$	$n = 46$	$n = 9$
non-scaled MHD Nrmse	0.50	0.64	0.29	0.14
scaled MHD nRMSE	0.41	0.56	0.21	0.17
Liu et al. (2016) nRMSE	0.40	0.32	0.12	0.35

Note. The nRMSE correspond to comparisons between "n" PSD pairs of measured and simulated data for the fixed L^* shells at epoch times within $0 \le Ep \le 10$ hr for Case 1 and $0 \le Ep \le 13$ hr for Case 2.

unscaled- and scaled-D_{LL}[MHD] at both fixed L^* shells (see panels b4–b5) since the scaling factor is close to one. Also in panels a4–a5 and b4–b5, D_{LL}[LIU] is seen to outperform scaled-D_{LL}[MHD] for capturing the dropouts at $L^* = 4.3$ during Case 1 and at $L^* = 4.9$ in Case 2; however, it underestimates PSD at $L^* = 4.3$ for Case 2. And taking into account the uncertainty of the PSD results from scaled-D_{LL}[MHD] (gray areas), it can be seen in both case studies that the uncertainties in simulated PSD associated with the D_{LL} model increase during the dropouts. This result shows that the 1D simulations are very sensitive to assumed D_{LL} magnitude during the dropouts due to fast radial diffusion dynamics imposed by the outer boundary conditions, which reflect the enhanced losses at geosynchronous orbit over this interval (see Figures S2 and S3). This explains why simulations with D_{LL}[LIU] (blue curves) that is ~10–30 times larger than non-scaled-D_{LL}[MHD] during the dropouts (Figures 5b–5c) roughly align with the lower limit of the gray areas in both L^* shells. On the contrary, it is interesting to note after Ep = 16 hr in panels a4–a5 that the uncertainty of the modeled PSD reduced significantly during the recovery phase of Case 1.

To quantify the performance of each D_{LL} input coefficient in dropout modeling, Table 1 presents a comparison of the normalized root mean square error

(nRMSE) between measured and simulated PSD at $L^* = 4.3$ and $L^* = 4.9$. The nRMSE values were calculated as in Welling and Ridley (2010) and Jauer et al. (2019), where a smaller nRMSE means a better PSD prediction from the model. It is quantitatively proven in this table that the 1D simulations better solve the gradual dropout in Case 2 since the nRMSE values of this case are smaller overall. However, because D_{LL}[LIU] underestimates PSD at $L^* < 4.5$ in this case (see after Ep = 4 hr in panel b5 of Figure 10), its performance is the worst at lower L^* for Case 2. For Case 1, the nRMSE values indicate that the 1D simulations better solve the dropout at higher L^* regions ($L^* = 4.9$) for MHD-D_{LL} models, while D_{LL}[LIU] shows better performance regarding the deep loss at $L^* = 4.3$. Generally, the scaled MHD-D_{LL} improved the simulation results for the two case studies and at both high and low L^* regions, except for Case 2 in $L^* = 4.3$ where the performance is slightly lower than for the non-scaled-D_{LL}[MHD]. This is also where the performance of scaled-D_{LL}[MHD] outperforms that of D_{LL}[LIU].

5. Discussion and Conclusions

In this work, we computed event-specific D_{LL} coefficients using MHD simulations to study their contribution to deep (Case 1) and non-deep (Case 2) dropouts related to CIR storms. In an attempt to obtain a more realistic storm-time D_{LL}, D_{LL}[MHD] was scaled for both event studies using in situ ULF wave power observations by RBSP-B. The diffusion simulations executed for equatorially mirroring electrons with $\mu = 700$ MeV/G and using scaled-D_{LL}[MHD] greatly improved the solution of the Case 1 strong dropout compared to that obtained with non-scaled-D_{LL}[MHD]. However, the diffusion model with scaled-D_{LL}[MHD] did not fully resolve the deep loss down to $L^* < 4.5$ on 27 March 2017 during Case 1. In turn, the less-abrupt Case 2 dropout on 21 November 2017 was well captured across the outer belt in the 1D simulations with non-scaled-D_{LL}[MHD] and scaled-D_{LL}[MHD] coefficients. The deep dropout at $L^* < 4.5$ in Case 1, which was under-reproduced by simulation with scaled-D_{LL}[MHD], was better captured by the simulation with empirical D_{LL}[LIU]. However, D_{LL}[LIU] overestimated the losses in the same region for Case 2. Furthermore, we have also presented the uncertainty in modeled PSD associated with the uncertainty in scaled-D_{LL}[MHD]. It was verified that the uncertainty around the PSD results obtained from scaled-D_{LL}[MHD] increases significantly during the dropouts of both case studies, with lower limits of these PSD results being as low as those from using D_{LL}[LIU]. It is interesting to see in Figure 10 (panel a5) that a possible mean ratio larger than ∼3 could cause the 1D simulation to capture most of the deep dropout at $L^* < 4.5$ as indicated by the PSD uncertainty from using scaled-D_{LL}[MHD]. Therefore, taking into account the uncertainty of the diffusion simulation results obtained for scaled-D_{LL}[MHD], it is possible that magnetopause shadowing combined with outward radial diffusion could still explain and dominate the fast dropout of MeV electrons below $L^* = 4.5$ in Case 1. This loss scenario is supported by many previous works exploring the role of fast outward radial diffusion to explain flux dropouts of the core (high equatorial pitch angle) radiation belt electron populations even at multi-MeV energies (e.g., Mann et al. (2016); Mann et al. (2018); Olifer et al. (2018); Ozeke et al. (2020); Pinto et al. (2020)).

Besides, the rescaling of D_{LL}[MHD] in Case 1 was based on Van Allen Probe B ULF-E_ϕ power observations on 27 March (from 06:30 UT to 09:30UT) that were taken at L ranging from 6 to 4.5 (Figures 8e–8g, corresponding to L^* values from 5.3 to 4.1). Meanwhile, the ongoing Case 1 dropout that started at ∼4 UT (Ep = 0 hr) on this day was observed by Van Allen Probes at $L = 5$ in Figure 4d and even below $L = 4.5$, as discussed in Figure 1. The actual ratio of real to MHD ULF wave power could have been higher at $L < 6$ with the onset of the main phase of the storm before 06:30 UT. Previous studies have shown that ULF wave power is strongly enhanced during the storm main phase nearly down to the plasmapause (Hartinger et al., 2010; Ozeke et al., 2020; Pinto et al., 2020; Rae et al., 2019; Ren et al., 2017). For example, Pinto et al. (2020) showed for several events in 2012–2017 that very strong ULF power was often measured on the ground at $L \sim 4$ between the time of minimum LCDS and the time of maximum flux dropout. They showed that such ULF wave activity yields corresponding D_{LL} magnitudes of ∼ 1/day in situ, that is, more than 10 times larger than our peak D_{LL}[MHD] found at $L = 4$ (cf. Figure 4b at Ep ∼ 0 hr, for the solid red line). However, the ULF wave power comparison is not performed before 06:30 UT in Figures 8 and 9 since the electric field data provided by Van Allen Probe B was very noisy through this period. Moreover, Van Allen Probe B ULF wave data were obtained in a very narrow MLT domain near 20 MLT in the dusk sector, where ULF wave power could have been much lower than elsewhere on the nightside. Therefore, most of the dropouts at $L < 5.5$ could be due to ULF waves present at ∼04–06 UT, possibly at other MLTs than the domain covered by the Van Allen Probes during this event. Considering these additional uncertainties in the scaled-D_{LL}[MHD], it is conceivable that stronger outward radial diffusion could have been present during Case 1, explaining the steeper measured dropout than obtained in the simulations.

In addition to the uncertainty of scaled-D_{LL}[MHD], uncertainty related to the LCDS results derived with the TS04 magnetic field model could also lead to uncertainties in the simulated PSD. The LCDS results were only implemented in the 1D simulations of Case 1. According to analysis by Albert et al. (2018), the uncertainty of the minimum LCDS position is mainly due to the magnetic field model and could be up to 0.7 R_E. On the other hand, the actual gradient of electron PSD could have been steeper than that simulated for Case 1, increasing outward diffusion and loss. It should be noted that the Van Allen Probes measurements used for the initial PSD gradient are limited in time accuracy (e.g., Olifer et al. (2021)) due to the 4-hr time steps of data acquisition within $L^* = 3 - 6$. Furthermore, updating the outer boundary condition at $L^* = 6$ with GOES data does not guarantee that the simulated PSD gradient was equivalent to the real one in that L^* domain at an instant of time since this gradient highly depends on the evolution of actual radial diffusion rates and also on the evolution of the actual and unknown PSD gradient near and just above $L^* = 6$ (Ozeke et al., 2018).

The other major loss mechanism commonly suggested for main phase flux dropouts is EMIC wave scattering, which promotes electron losses through precipitation into the atmosphere (e.g., Blum et al., 2015; Usanova et al., 2014; Xiang et al., 2017, 2018). Previous long-term (Drozdov et al., 2015, 2017) and event-specific (Shprits et al., 2016) 3D diffusion simulations with VERB code, as well as observational works by Shprits et al. (2017, 2018), found that EMIC scattering loss is mostly required to simulate fast dropouts of electron populations in μ regimes of a few thousand MeV/G, which is higher than the μ value studied here. Recent studies have explained that for electrons with kinetic energy below the typical minimum resonant energy of >2 MeV (i.e., $\mu > 1000$ MeV/G), EMIC waves generally cannot efficiently scatter those of high equatorial pitch angles (i.e., $K \sim 0\ R_E G^{1/2}$), whereas <2 MeV electrons with low pitch angles can indeed be scattered (e.g., Cao et al., 2017; Ross et al., 2021). Thus, additional resonant interactions with hiss and chorus waves are required to account for the scattering of the core high-pitch angle populations at lower energies down to the loss cone (e.g., Mourenas et al., 2016; Zhang et al., 2017). Moreover, in order for EMIC waves to operate together with the other waves in producing <2 MeV electron dropouts, these EMIC waves must have very high and unusual frequencies close to the helium gyrofrequency, or a wave frequency to proton gyrofrequency ratio >0.5. Such high-frequency EMIC waves have been found within regions of high-density plasma, such as the plasmasphere or a plume, but because they are comparatively rare EMIC wave-driven dropouts below 2 MeV are relatively unlikely (Kersten et al., 2014; Mourenas et al., 2016; Ross et al., 2021). However, an analysis of 16 years of electron flux dropouts recorded by GPS satellites suggested that a finite fraction of the ∼1–2 MeV dropouts recorded near $L = 4.2$ could indeed be related to combined EMIC and chorus or hiss wave-driven precipitation (Boynton et al., 2017).

Concerning additional limitations of the present work, the outer boundary conditions were fixed at $L^* = 6$ from calibrated PSD data, acquired at geosynchronous orbit in a range of $5 < L^* < 6$. Test runs with this boundary fixed at $L^* = 5.5$ showed very similar results for all 1D simulations (not included in the paper). On the other hand, the scale factor to correct MHD-D_{LL} relative to RBSP-B average wave power observations in Case 1 was derived from an interval of MHD validations on the nightside, while the corresponding factor for Case 2 was derived from a dayside interval. The nightside magnetosphere must also be taken into account for the scale factor calculation of Case 2 to be consistent with the scale factor derivation in Case 1, given that MHD simulations can highly underestimate the ULF waves in this sector (as per seen in Figure 8 for Case 1). However, the 1D simulations in Figure 10 indicated that the small factor of 1.37 in MHD-D_{LL} of Case 2 is sufficient to simulate the event throughout the outer belt during the electron dropout. Another limitation concerning scaled-D_{LL}[MHD] relies on such mean scaling factors being constant through the 1D simulation intervals. As indicated in Figures 9a and 9b (though not explicitly), the data-to-MHD average power ratio can be time-dependent. With due caution, a time-dependent scale factor would possibly have produced more reliable PSD results for the dropouts (within the uncertainty range) from the 1D simulations with scaled-D_{LL}[MHD]. This is challenging considering the satellite is also moving in L and a global validation of the MHD fields with a constellation of satellites is needed.

Despite all these limitations, the comprehensive radial diffusion analysis performed here to model relativistic electron losses in the outer radiation belt (up to $L^* = 6$) during moderate geomagnetic storms revealed that outward radial diffusion driven by ULF waves is a dominant loss mechanism for non-deep and smooth electron dropouts. On the other hand, radial diffusion rates due to ULF waves are generally more enhanced and reach low L shells in deeper and stronger dropouts, consistent with fast outward diffusion also dominant down to $L^* < 4.5$. Nevertheless, it has been argued that relatively higher ULF wave power than simulated with MHD is required to model this deep dropout effectively. This work demonstrates that the role of loss mechanisms for ∼ MeV electron

dropouts under moderate geomagnetic activity, such as those driven by CIR storms, is relatively well understood. However, further coordinated modeling of the outer electron radiation belt during other case studies for this type of event is needed to improve the accuracy of diffusion simulation inputs such as the storm-time D_{LL}.

Data Availability Statement

The Van Allen Probes data from the ECT, EMFISIS and EFW suites are publicly available at (https://rbsp-ect.newmexicoconsortium.org/rbsp_ect.php), (https://emfisis.physics.uiowa.edu/), and (http://www.space.umn.edu/missions/rbspefw-home-university-of-minnesota/), respectively. The GOES-15 data from the MAGED instrument are available at (https://www.ngdc.noaa.gov/stp/satellite/goes/dataaccess.html). Data for solar wind and geomagnetic indices (SYM-H, AE, and *Kp*) were collected from NASA's GSFC SPDF OMNIWeb (https://omniweb.gsfc.nasa.gov/).

Acknowledgments
We thank the Brazilian Ministry of Science, Technology and Innovation, and the Brazilian Space Agency. G. B. D. Silva thanks to CNPq for grants 143011/2017-0, 317953/2021-4, and 300282/2022-2, and to CAPES-PrInt for grant 88887.363809/2019-00. L. R. Alves thanks for financial support by CNPq through PQ-grant number 309026/2021-0. W. Tu thanks the financial support by NSF Grant AGS 1752736 and NASA Grants 80NSSC19K0908, 80NSSC21K1312, and 80NSSC21K2008. V. M. Souza thanks to CNPq for Grant 300342/2022-5. MHD simulation results have been provided by the Community Coordinated Modeling Center at Goddard Space Flight Center through their public Runs on Request system (http://ccmc.gsfc.nasa.gov). The SWMF/BATSRUS Model was developed by the Center for Space Environment Modeling (CSEM) at the University of Michigan. The authors are thankful to the development teams of Spacepy (https://pythonhosted.org/SpacePy/), IRBEM-LIB (http://craterre.onecert.fr/prbem/irbem/description.html), and LANLGeoMag (https://github.com/drsteve/LANLGeoMag).

References

Albert, J. M., Selesnick, R., Morley, S. K., Henderson, M. G., & Kellerman, A. (2018). Calculation of last closed drift shells for the 2013 gem radiation belt challenge events. *Journal of Geophysical Research: Space Physics*, *123*(11), 9597–9611. https://doi.org/10.1029/2018ja025991

Ali, A. F., Malaspina, D. M., Elkington, S. R., Jaynes, A. N., Chan, A. A., Wygant, J., & Kletzing, C. A. (2016). Electric and magnetic radial diffusion coefficients using the van allen probes data. *Journal of Geophysical Research: Space Physics*, *121*(10), 9586–9607. Retrieved from https://doi.org/10.1002/2016ja023002

Alves, L. R., Da Silva, L. A., Souza, V. M., Sibeck, D. G., Jauer, P. R., Vieira, L. E. A., et al.(2016). Outer radiation belt dropout dynamics following the arrival of two interplanetary coronal mass ejections. *Geophysical Research Letters*, *43*(3), 978–987. Retrieved from https://doi.org/10.1002/2015gl067066

Alves, L. R., Souza, V. M., Jauer, P. R., da Silva, L. A., Medeiros, C., Braga, C. R., et al. (2017). The role of solar wind structures in the generation of ulf waves in the inner magnetosphere. *Solar Physics*, *292*(7), 92. Retrieved from https://doi.org/10.1007/s11207-017-1113-4

Baker, D. N., Erickson, P., Fennell, J. F., Coster, J. C., Jaynes, A. N., & Verronen, P. T. (2018). Space weather effects in the earth's radiation belts. *Space Science Reviews*, *214*(17). https://doi.org/10.1007/s11214-017-0452-7

Baker, D. N., Kanekal, S. G., Hoxie, V. C., Batiste, S., Bolton, M., Li, X., et al. (2013). The relativistic electron-proton telescope (rept) instrument on board the radiation belt storm probes (rbsp) spacecraft: Characterization of earth's radiation belt high-energy particle populations. *Space Science Reviews*, *179*(1), 337–381. Retrieved from https://doi.org/10.1007/s11214-012-9950-9

Barani, M., Tu, W., Sarris, T., Pham, K., & Redmon, R. J. (2019). Estimating the azimuthal mode structure of ulf waves based on multiple goes satellite observations. *Journal of Geophysical Research: Space Physics*, *124*(7), 5009–5026. Retrieved from https://doi.org/10.1029/2019ja026927

Blake, J., Carranza, P., Claudepierre, S., Clemmons, J., Crain, W., Dotan, Y., et al. (2013). *The magnetic electron ion spectrometer (mageis) instruments aboard the radiation belt storm probes (rbsp) spacecraft*. In *The Van Allen Probes Mission* (pp. 383–421). Springer. https://doi.org/10.1007/978-1-4899-7433-4_12

Blum, L., Li, X., & Denton, M. (2015). Rapid mev electron precipitation as observed by sampex/hilt during high-speed stream-driven storms. *Journal of Geophysical Research: Space Physics*, *120*(5), 3783–3794. Retrieved from https://doi.org/10.1002/2014ja020633

Boscher, D., Bourdarie, S., O'Brien, P., & Guild, T. (2012). Irbem library, version 4.4.0. Retrieved from http://sourceforge.net/projects/irbem/

Boynton, R. J., Mourenas, D., & Balikhin, M. A. (2017). Electron flux dropouts at l 4.2 from global positioning system satellites: Occurrences, magnitudes, and main driving factors. *Journal of Geophysical Research: Space Physics*, *122*(11), 11428–11441. https://doi.org/10.1002/2017JA024523

Brautigam, D., & Albert, J. (2000). Radial diffusion analysis of outer radiation belt electrons during the october 9, 1990, magnetic storm. *Journal of Geophysical Research*, *105*(A1). https://doi.org/10.1029/1999JA900344

Cao, X., Shprits, Y. Y., Ni, B., & Zhelavskaya, I. S. (2017). Scattering of ultra-relativistic electrons in the van allen radiation belts accounting for hot plasma effects. *Scientific Reports*, *7*(1), 1–7. Retrieved from https://doi.org/10.1038/s41598-017-17739-7

Chen, Y., Friedel, R., & Reeves, G. (2006). Phase space density distributions of energetic electrons in the outer radiation belt during two geospace environment modeling inner magnetosphere/storms selected storms. *Journal of Geophysical Research*, *111*(A11). https://doi.org/10.1029/2006ja011703

Drozdov, A. Y., Shprits, Y. Y., Orlova, K. G., Kellerman, A. C., Subbotin, D. A., Baker, D. N., et al. (2015). Energetic, relativistic, and ultrarelativistic electrons: Comparison of long-term verb code simulations with van allen probes measurements. *Journal of Geophysical Research: Space Physics*, *120*(5), 3574–3587. Retrieved from https://doi.org/10.1002/2014JA020637

Drozdov, A. Y., Shprits, Y. Y., Usanova, M. E., Aseev, N. A., Kellerman, A. C., & Zhu, H. (2017). Emic wave parameterization in the long-term verb code simulation. *Journal of Geophysical Research: Space Physics*, *122*(8), 8488–8501. https://doi.org/10.1002/2017ja024389

Elkington, S. R. (2006). A review of ulf interactions with radiation belt electrons. In *Magnetospheric ulf waves: Synthesis and new directions* (pp. 177–193). American Geophysical Union (AGU). https://doi.org/10.1029/169GM12

Falthammar, C.-G. (1965). Effects of time-dependent electric fields on geomagnetically trapped radiation. *Journal of Geophysical Research*, *70*(11), 2503–2516. https://doi.org/10.1029/jz070i011p02503

Fei, Y., Chan, A. A., Elkington, S. R., & Wiltberger, M. J. (2006). Radial diffusion and mhd particle simulations of relativistic electron transport by ulf waves in the september 1998 storm. *Journal of Geophysical Research*, *111*(A12). Retrieved from https://doi.org/10.1029/2005ja011211

Fok, M.-C., Buzulukova, N. Y., Chen, S.-H., Glocer, A., Nagai, T., Valek, P., & Perez, J. D. (2014). The comprehensive inner magnetosphere-ionosphere model. *Journal of Geophysical Research: Space Physics*, *119*(9), 7522–7540. Retrieved from https://doi.org/10.1002/2014ja020239

Green, J. C., & Kivelson, M. (2004). Relativistic electrons in the outer radiation belt: Differentiating between acceleration mechanisms. *Journal of Geophysical Research*, *109*(A3). https://doi.org/10.1029/2003ja010153

Hartinger, M., Moldwin, M. B., Angelopoulos, V., Takahashi, K., Singer, H. J., Anderson, R. R., et al. (2010). Pc5 wave power in the quiet-time plasmasphere and trough: Crres observations. *Geophysical Research Letters*, *37*(7). Retrieved from https://doi.org/10.1029/2010gl042475

Huang, C.-L., Spence, H. E., Hudson, M. K., & Elkington, S. R. (2010). Modeling radiation belt radial diffusion in ulf wave fields: 2. Estimating rates of radial diffusion using combined mhd and particle codes. *Journal of Geophysical Research*, *115*(A6). https://doi.org/10.1029/2009JA014918

Hudson, M. K., Baker, D. N., Goldstein, J., Kress, B. T., Paral, J., Toffoletto, F. R., & Wiltberger, M. (2014). Simulated magnetopause losses and van allen probe flux dropouts. *Geophysical Research Letters*, *41*(4), 1113–1118. Retrieved from https://doi.org/10.1002/2014gl059222

Hudson, M. K., Brito, T., Elkington, S., Kress, B., Li, Z., & Wiltberger, M. (2012). Radiation belt 2d and 3d simulations for cir-driven storms during Carrington rotation 2068. *Journal of Atmospheric and Solar-Terrestrial Physics*, *83*, 51–62. https://doi.org/10.1016/j.jastp.2012.03.017

Hudson, M. K., Elkington, S. R., Li, Z., Patel, M., Pham, K., Sorathia, K., et al. (2021). Mhd-test particles simulations of moderate cme and cir-driven geomagnetic storms at solar minimum. *Space Weather*, *19*(12), e2021SW002882. Retrieved from https://doi.org/10.1029/2021sw002882

Jacobs, J., Kato, Y., Matsushita, S., & Troitskaya, V. (1964). Classification of geomagnetic micropulsations. *Journal of Geophysical Research*, *69*(1), 180–181. https://doi.org/10.1029/jz069i001p00180

Jauer, P. R., Wang, C., Souza, V., Alves, M., Alves, L., Pádua, M., et al. (2019). A global magnetohydrodynamic simulation study of ultra-low-frequency wave activity in the inner magnetosphere: Corotating interaction region+ alfvénic fluctuations. *The Astrophysical Journal*, *886*(1), 59. https://doi.org/10.3847/1538-4357/ab4db5

Jaynes, A. N., Baker, D. N., Singer, H. J., Rodriguez, J. V., Loto'aniu, T. M., Ali, A. F., et al. (2015). Source and seed populations for relativistic electrons: Their roles in radiation belt changes. *Journal of Geophysical Research: Space Physics*, *120*, 7240–7254. https://doi.org/10.1002/2015ja021234

Kersten, T., Horne, R. B., Glauert, S. A., Meredith, N. P., Fraser, B. J., & Grew, R. S. (2014). Electron losses from the radiation belts caused by emic waves. *Journal of Geophysical Research: Space Physics*, *119*(11), 8820–8837. Retrieved from https://doi.org/10.1002/2014ja020366

Kletzing, C., Kurth, W., Acuna, M., MacDowall, R., Torbert, R., Averkamp, T., et al. (2013). The electric and magnetic field instrument suite and integrated science (emfisis) on rbsp. *Space Science Reviews*, *179*(1–4), 127–181. https://doi.org/10.1007/978-1-4899-7433-4_5

Lejosne, S., & Kollmann, P. (2020). Radiation belt radial diffusion at earth and beyond. *Space Science Reviews*, *216*(19). Retrieved from https://doi.org/10.1007/s11214-020-0642-6

Li, L.-F., Tu, W., Dai, L. T. B.-B., Wang, C., & Barani, M. (2020). Quantifying event-specific radial diffusion coefficients of radiation belt electrons with the ppmlr-mhd simulation. *Journal of Geophysical Research: Space Physics*, *125*(5), e2019JA027634. Retrieved from https://doi.org/10.1029/2019ja027634

Li, Z., Hudson, M. K., Jaynes, A., Boyd, A., Malaspina, D., Thaller, S., et al. (2014). Modeling gradual diffusion changes in radiation belt electron phase space density for the march 2013 van allen probes case study. *Journal of Geophysical Research: Space Physics*, *119*(10), 8396–8403. Retrieved from https://doi.org/10.1002/2014JA020359

Li, Z., Hudson, M. K., Paral, J., Wiltberger, M., & Turner, D. L. (2016). Global ulf wave analysis of radial diffusion coefficients using a global mhd model for the 17 march 2015 storm. *Journal of Geophysical Research: Space Physics*, *121*(7), 6196–6206. Retrieved from https://doi.org/10.1002/2016ja022508

Li, Z., Hudson, M. K., Patel, M., Wiltberger, M., Boyd, A., & Turner, D. L. (2017). Ulf wave analysis and radial diffusion calculation using a global mhd model for the 17 march 2013 and 2015 storms. *Journal of Geophysical Research: Space Physics*, *122*(7), 7353–7363. https://doi.org/10.1002/2016ja023846

Liu, W., Tu, W., Li, X., Sarris, T., Khotyaintsev, Y., Fu, H., et al. (2016). On the calculation of electric diffusion coefficient of radiation belt electrons with in situ electric field measurements by themis. *Geophysical Research Letters*, *43*(3), 1023–1030. Retrieved from https://doi.org/10.1002/2015gl067398

Loto'Aniu, T., Singer, H., Waters, C., Angelopoulos, V., Mann, I. R., Elkington, S., & Bonnell, J. (2010). Relativistic electron loss due to ultralow frequency waves and enhanced outward radial diffusion. *Journal of Geophysical Research*, *115*(A12).

Mann, I. R., Ozeke, L., Morley, S., Murphy, K. R., Claudepierre, S., Turner, D., et al.(2018). Reply to 'the dynamics of van allen belts revisited'. *Nature Physics*, *14*(2), 103–104. Retrieved from https://doi.org/10.1038/nphys4351

Mann, I. R., Ozeke, L., Murphy, K. R., Claudepierre, S. G., Turner, D. L., Baker, D. N., et al. (2016). Explaining the dynamics of the ultra-relativistic third van allen radiation belt. *Nature Physics*, *12*(10), 978–983. Retrieved from https://doi.org/10.1038/nphys3799

McIlwain, C. E. (1961). Coordinates for mapping the distribution of magnetically trapped particles. *Journal of Geophysical Research*, *66*(11), 3681–3691. https://doi.org/10.1029/jz066i011p03681

McPherron, R., Baker, D., & Crooker, N. (2009). Role of the russell–mcpherron effect in the acceleration of relativistic electrons. *Journal of Atmospheric and Solar-Terrestrial Physics*, *71*(10–11), 1032–1044. https://doi.org/10.1016/j.jastp.2008.11.002

Medeiros, C., Souza, V., Vieira, L., Sibeck, D., Halford, A., Kang, S.-B., et al. (2019). On the contribution of emic waves to the reconfiguration of the relativistic electron butterfly pitch angle distribution shape on 2014 september 12—A case study. *The Astrophysical Journal*, *872*(1), 36. https://doi.org/10.3847/1538-4357/aaf970

Morley, S. K., Friedel, R. H. W., Spanswick, E. L., Reeves, G. D., Steiberg, J. T., Koller, J., et al. (2010). Dropouts of the outer electron radiation belt in response to solar wind stream interfaces: Global positioning system observations. *Proceedings of the Royal Society A*, *466*, 3329–3350. https://doi.org/10.1098/rspa.2010.0078

Mourenas, D., Artemyev, A. V., Ma, Q., Agapitov, O. V., & Li, W. (2016). Fast dropouts of multi-mev electrons due to combined effects of emic and whistler mode waves. *Geophysical Research Letters*, *43*(9), 4155–4163. Retrieved from https://doi.org/10.1002/2016gl068921

O'Brien, T. P., & Moldwin, M. B. (2003). Empirical plasmapause models from magnetic indices. *Geophysical Research Letters*, *30*(4). Retrieved from https://doi.org/10.1029/2002GL016007

Olifer, L., Mann, I. R., Morley, S. K., Ozeke, L. G., & Choi, D. (2018). On the role of last closed drift shell dynamics in driving fast losses and van allen radiation belt extinction. *Journal of Geophysical Research: Space Physics*, *123*(5), 3692–3703. https://doi.org/10.1029/2018ja025190

Olifer, L., Mann, I. R., Ozeke, L. G., Claudepierre, S. G., Baker, D. N., & Spence, H. E. (2021). On the similarity and repeatability of fast radiation belt loss: Role of the last closed drift shell. *Journal of Geophysical Research: Space Physics*, *126*(11), e2021JA029957. Retrieved from https://doi.org/10.1029/2021ja029957

Olifer, L., Mann, I. R., Ozeke, L. G., Rae, I. J., & Morley, S. K. (2019). On the relative strength of electric and magnetic ulf wave radial diffusion during the march 2015 geomagnetic storm. *Journal of Geophysical Research: Space Physics*, *124*(4), 2569–2587. Retrieved from https://doi.org/10.1029/2018ja026348

Orlova, K., Spasojevic, M., & Shprits, Y. Y. (2014). Activity-dependent global model of electron loss inside the plasmasphere. *Geophysical Research Letters*, *41*(11), 3744–3751. https://doi.org/10.1002/2014gl060100

Ozeke, L. G., Mann, I. R., Murphy, K. R., Degeling, A. W., Claudepierre, S. G., & Spence, H. E. (2018). Explaining the apparent impenetrable barrier to ultra-relativistic electrons in the outer van allen belt. *Nature Communications*, *9*(1), 1–11. https://doi.org/10.1038/s41467-018-04162-3

Ozeke, L. G., Mann, I. R., Murphy, K. R., Jonathan Rae, I., & Milling, D. K. (2014). Analytic expressions for ulf wave radiation belt radial diffusion coefficients. *Journal of Geophysical Research: Space Physics*, *119*(3), 1587–1605. Retrieved from https://doi.org/10.1002/2013ja019204

Ozeke, L. G., Mann, I. R., Murphy, K. R., Sibeck, D. G., & Baker, D. N. (2017). Ultra-relativistic radiation belt extinction and ulf wave radial diffusion: Modeling the September 2014 extended dropout event. *Geophysical Research Letters*, *44*(6), 2624–2633. Retrieved from https://doi.org/10.1002/2017gl072811

Ozeke, L. G., Mann, I. R., Olifer, L., Dufresne, K. Y., Morley, S. K., Claudepierre, S. G., et al. (2020). Rapid outer radiation belt flux dropouts and fast acceleration during the march 2015 and 2013 storms: The role of ultra-low frequency wave transport from a dynamic outer boundary. *Journal of Geophysical Research: Space Physics*, *125*(2), e2019JA027179. Retrieved from https://doi.org/10.1029/2019ja027179

Ozeke, L. G., Mann, I. R., Turner, D. L., Murphy, K. R., Degeling, A. W., Rae, I. J., & Milling, D. K. (2014). Modeling cross l shell impacts of magnetopause shadowing and ulf wave radial diffusion in the van allen belts. *Geophysical Research Letters*, *41*(19), 6556–6562. Retrieved from https://doi.org/10.1002/2014gl060787

Pham, K. H., Tu, W., & Xiang, Z. (2017). Quantifying the precipitation loss of radiation belt electrons during a rapid dropout event. *Journal of Geophysical Research: Space Physics*, *122*(10), 10287–10303. Retrieved from https://doi.org/10.1002/2017ja024519

Pinto, V. A., Zhang, X.-J., Mourenas, D., Bortnik, J., Artemyev, A. V., Lyons, L. R., & Moya, P. S. (2020). On the confinement of ultrarelativistic electron remnant belts to low shells. *Journal of Geophysical Research: Space Physics*, *125*(3), e2019JA027469. Retrieved from https://doi.org/10.1029/2019ja027469

Rae, I. J., Murphy, K. R., Watt, C. E., Sandhu, J. K., Georgiou, M., Degeling, A. W., et al. (2019). How do ultra-low frequency waves access the inner magnetosphere during geomagnetic storms? *Geophysical Research Letters*, *46*(19), 10699–10709. Retrieved from https://doi.org/10.1029/2019gl082395

Reeves, G. D., McAdams, K. L., & Friedel, R. H. W. (2003). Acceleration and loss of relativistic electrons during geomagnetic storms. *Geophysical Research Letters*, *30*(10), 1529. https://doi.org/10.1029/2002gl016513

Reeves, G. D., Spence, H. E., Henderson, M. G., Morley, S. K., Friedel, R. H. W., Funsten, H. O., & Baker, D. N. (2013). Electron acceleration in the heart of the van allen radiation belts. *Science*, *341*(6149). https://doi.org/10.1126/science.1237743

Ren, J., Zong, Q.-G., Miyoshi, Y., Zhou, X. Z., Wang, Y. F., Rankin, R., et al. (2017). Low-energy (<200 ev) electron acceleration by ulf waves in the plasmaspheric boundary layer: Van allen probes observation. *Journal of Geophysical Research: Space Physics*, *122*(10), 9969–9982. Retrieved from https://doi.org/10.1002/2017ja024316

Richardson, I. G. (2018). Solar wind stream interaction regions throughout the heliosphere. *Living Reviews in Solar Physics*, *15*. https://doi.org/10.1007/s41116-017-0011-z

Roederer, J. G. (1970). *Dynamics of geomagnetically trapped radiation*. Springer-Verlag.

Ross, J. P. J., Glauert, S. A., Horne, R. B., Watt, C. E. J., & Meredith, N. P. (2021). On the variability of emic waves and the consequences for the relativistic electron radiation belt population. *Journal of Geophysical Research: Space Physics*, *126*(12), e2021JA029754. Retrieved from https://doi.org/10.1029/2021ja029754

Sandhu, J. K., Rae, I. J., Wygant, J. R., Breneman, A. W., Tian, S., Watt, C. E. J., et al. (2021). Ulf wave driven radial diffusion during geomagnetic storms: A statistical analysis of van allen probes observations. *Journal of Geophysical Research: Space Physics*, *126*(4), e2020JA029024. Retrieved from https://doi.org/10.1029/2020ja029024

Schulz, M., & Lanzerotti, L. J. (1974). *Particle diffusion in the radiation belts*. In *Physics and Chemistry in Space* (Vol. 7). Springer-Verlag.

Shprits, Y. Y., Drozdov, A. Y., Spasojevic, M., Kellerman, A. C., Usanova, M. E., Engebretson, M. J., et al. (2016). Wave-induced loss of ultra-relativistic electrons in the van allen radiation belts. *Nature Communications*, *7*(1), 1–7. https://doi.org/10.1038/ncomms12883

Shprits, Y. Y., Elkington, S. R., Meredith, N. P., & Subbotin, D. A. (2008). Review of modeling of losses and sources of relativistic electrons in the outer radiation belt i: Radial transport. *Journal of Atmospheric and Solar-Terrestrial Physics*, *70*(14), 1679–1693. Retrieved from https://doi.org/10.1016/j.jastp.2008.06.008

Shprits, Y. Y., Horne, R. B., Kellerman, A. C., & Drozdov, A. Y. (2018). The dynamics of van allen belts revisited. *Nature Physics*, *14*(2), 102–103. https://doi.org/10.1038/nphys4350

Shprits, Y. Y., Kellerman, A., Aseev, N., Drozdov, A. Y., & Michaelis, I. (2017). Multi-mev electron loss in the heart of the radiation belts. *Geophysical Research Letters*, *44*(3), 1204–1209. https://doi.org/10.1002/2016gl072258

Shprits, Y. Y., Meredith, N. P., & Thorne, R. M. (2007). Parameterization of radiation belt electron loss timescales due to interactions with chorus waves. *Geophysical Research Letters*, *34*(11). https://doi.org/10.1029/2006gl029050

Shprits, Y. Y., Thorne, R., Friedel, R., Reeves, G., Fennell, J., Baker, D., & Kanekal, S. (2006). Outward radial diffusion driven by losses at magnetopause. *Journal of Geophysical Research*, *111*(A11). https://doi.org/10.1029/2006ja011657

Summers, D., Thorne, R. M., & Xiao, F. (1998). Relativistic theory of wave-particle resonant diffusion with application to electron acceleration in the magnetosphere. *Journal of Geophysical Research*, *103*(A9), 20487–20500. https://doi.org/10.1029/98ja01740

Thorne, R. M. (2010). Radiation belt dynamics: The importance of wave-particle interactions. *Geophysical Research Letters*, *37*(22). https://doi.org/10.1029/2010gl044990

Tóth, G., Holst, B. V. D., Sokolov, I. V., Zeeuw, D. L., Gombosi, T. I., Fang, F., et al. (2011). Adaptive numerical algorithms in space weather modeling. *Journal of Computational Physics*, *231*(3), 870.

Tóth, G., Sokolov, I. V., Gombosi, T. I., Chesney, D. R., Clauer, C. R., De Zeeuw, D. L., et al. (2005). Space weather modeling framework: A new tool for the space science community. *Journal of Geophysical Research*, *110*(A12). https://doi.org/10.1029/2005ja011126

Tsurutani, B. T., Gonzalez, W. D., Gonzalez, A. L. C., Guarnieri, F. L., Gopalswamy, N., Grande, M., et al. (2006). Corotating solar wind streams and recurrent geomagnetic activity: A review. *Journal of Geophysical Research*, *111*(A07S01). https://doi.org/10.1029/2005ja011273

Tsyganenko, N., & Sitnov, M. (2005). Modeling the dynamics of the inner magnetosphere during strong geomagnetic storms. *Journal of Geophysical Research*, *110*(A3). https://doi.org/10.1029/2004ja010798

Tu, W., Cunningham, G., Chen, Y., Morley, S. K., Reeves, G., Blake, J., et al. (2014). Event-specific chorus wave and electron seed population models in dream3d using the van allen probes. *Geophysical Research Letters*, *41*(5), 1359–1366. https://doi.org/10.1002/2013gl058819

Tu, W., Elkington, S. R., Li, X., Liu, W., & Bonnell, J. (2012). Quantifying radial diffusion coefficients of radiation belt electrons based on global mhd simulation and spacecraft measurements. *Journal of Geophysical Research*, *117*(A10). Retrieved from https://doi.org/10.1029/2012ja017901

Tu, W., Li, X., Chen, Y., Reeves, G., & Temerin, M. (2009). Storm-dependent radiation belt electron dynamics. *Journal of Geophysical Research*, *114*(A2). https://doi.org/10.1029/2008ja013480

Tu, W., Selesnick, R., Li, X., & Looper, M. (2010). Quantification of the precipitation loss of radiation belt electrons observed by sampex. *Journal of Geophysical Research*, *115*(A7). Retrieved from https://doi.org/10.1029/2009ja014949

Tu, W., Xiang, Z., & Morley, S. K. (2019). Modeling the magnetopause shadowing loss during the june 2015 dropout event. *Geophysical Research Letters*, *46*(16), 9388–9396. https://doi.org/10.1029/2019gl084419

Turner, D. L., Kilpua, E. K. J., Hietala, H., Claudepierre, S. G., O'Brien, T. P., Fennell, J. F., et al. (2019). The response of earth's electron radiation belts to geomagnetic storms: Statistics from the van allen probes era including effects from different storm drivers. *Journal of Geophysical Research: Space Physics*, *124*(2), 1013–1034. https://doi.org/10.1029/2018ja026066

Turner, D. L., Morley, S. K., Miyoshi, Y., Ni, B., & Huang, C.-L. (2012). Outer radiation belt flux dropouts: Current understanding and unresolved questions. In *Dynamics of the earth's radiation belts and inner magnetosphere* (pp. 195–212). American Geophysical Union (AGU). Retrieved from https://doi.org/10.1029/2012GM001310

Turner, D. L., Shprits, Y. Y., Hartinger, M., & Angelopoulos, V. (2012). Explaining sudden losses of outer radiation belt electrons during geomagnetic storms. *Nature Physics*, *8*(3), 208–212. Retrieved from https://doi.org/10.1038/nphys2185

Usanova, M. E., Drozdov, A. Y., Orlova, K., Mann, I. R., Shprits, Y., Robertson, M. T., et al. (2014). Effect of emic waves on relativistic and ultrarelativistic electron populations: Ground-based and van allen probes observations. *Geophysical Research Letters*, *41*(5), 1375–1381. https://doi.org/10.1002/2013GL059024

Welling, D. T., & Ridley, A. J. (2010). Validation of swmf magnetic field and plasma. *Space Weather*, *8*(3). https://doi.org/10.1029/2009sw000494

Wygant, J., Bonnell, J., Goetz, K., Ergun, R., Mozer, F., Bale, S. D., et al. (2013). *The electric field and waves instruments on the radiation belt storm probes mission*, (pp. 183–220). The Van Allen Probes Mission. https://doi.org/10.1007/978-1-4899-7433-4_6

Xiang, Z., Tu, W., Li, X., Ni, B., Morley, S. K., & Baker, D. N. (2017). Understanding the mechanisms of radiation belt dropouts observed by van allen probes. *Journal of Geophysical Research*, *122*(10), 9858–9879. https://doi.org/10.1002/2017ja024487

Xiang, Z., Tu, W., Ni, B., Henderson, M., & Cao, X. (2018). A statistical survey of radiation belt dropouts observed by van allen probes. *Geophysical Research Letters*, *45*(16), 8035–8043. https://doi.org/10.1029/2018gl078907

Yu, Y., Koller, J., & Morley, S. K. (2013). Quantifying the effect of magnetopause shadowing on electron radiation belt dropouts. *Annales Geophysicae*, *31*(11), 1929–1939. Retrieved from https://doi.org/10.5194/angeo-31-1929-2013

Yuan, C., & Zong, Q. (2013). The double-belt outer radiation belt during cme- and cir-driven geomagnetic storms. *Journal of Geophysical Research: Space Physics*, *118*(10), 6291–6301. Retrieved from https://doi.org/10.1002/jgra.50564

Yuan, C.-J., Zong, Q.-G., Wan, W.-X., Zhang, H., & Du, A.-M. (2015). Relativistic electron flux dropouts in the outer radiation belt associated with corotating interaction regions. *Journal of Geophysical Research: Space Physics*, *120*(9), 7404–7415. https://doi.org/10.1002/2015ja021003

Zhang, X.-J., Mourenas, D., Artemyev, A. V., Angelopoulos, V., & Thorne, R. M. (2017). Contemporaneous emic and whistler mode waves: Observations and consequences for mev electron loss. *Geophysical Research Letters*, *44*(16), 8113–8121. Retrieved from https://doi.org/10.1002/2017gl073886